https://ntrs.nasa.gov/search.jsp?R=20180003199 2019-08-31T16:31:59+00:00Z

NASA-TM-2018-219820

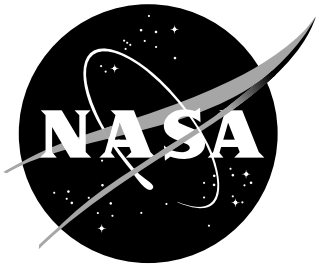

# Development and Documentation of kL-Based Linear, Nonlinear, and Full Reynolds Stress Turbulence Models

*Khaled S. Abdol-Hamid*
*Langley Research Center, Hampton, Virginia*

April 2018

## NASA STI Program . . . in Profile

Since its founding, NASA has been dedicated to the advancement of aeronautics and space science. The NASA scientific and technical information (STI) program plays a key part in helping NASA maintain this important role.

The NASA STI program operates under the auspices of the Agency Chief Information Officer. It collects, organizes, provides for archiving, and disseminates NASA's STI. The NASA STI program provides access to the NTRS Registered and its public interface, the NASA Technical Reports Server, thus providing one of the largest collections of aeronautical and space science STI in the world. Results are published in both non-NASA channels and by NASA in the NASA STI Report Series, which includes the following report types:

- TECHNICAL PUBLICATION. Reports of completed research or a major significant phase of research that present the results of NASA Programs and include extensive data or theoretical analysis. Includes compilations of significant scientific and technical data and information deemed to be of continuing reference value. NASA counter-part of peer-reviewed formal professional papers but has less stringent limitations on manuscript length and extent of graphic presentations.

- TECHNICAL MEMORANDUM. Scientific and technical findings that are preliminary or of specialized interest, e.g., quick release reports, working papers, and bibliographies that contain minimal annotation. Does not contain extensive analysis.

- CONTRACTOR REPORT. Scientific and technical findings by NASA-sponsored contractors and grantees.

- CONFERENCE PUBLICATION. Collected papers from scientific and technical conferences, symposia, seminars, or other meetings sponsored or co-sponsored by NASA.

- SPECIAL PUBLICATION. Scientific, technical, or historical information from NASA programs, projects, and missions, often concerned with subjects having substantial public interest.

- TECHNICAL TRANSLATION. English-language translations of foreign scientific and technical material pertinent to NASA's mission.

Specialized services also include organizing and publishing research results, distributing specialized research announcements and feeds, providing information desk and personal search support, and enabling data exchange services.

For more information about the NASA STI program, see the following:

- Access the NASA STI program home page at http://www.sti.nasa.gov

- E-mail your question to help@sti.nasa.gov

- Phone the NASA STI Information Desk at 757-864-9658

- Write to:
  NASA STI Information Desk
  Mail Stop 148
  NASA Langley Research Center
  Hampton, VA 23681-2199

NASA-TM-2018-219820

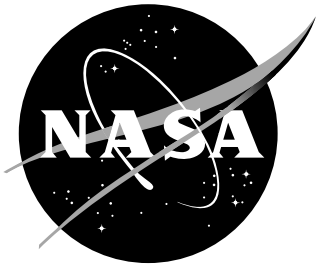

# Development and Documentation of kL-Based Linear, Nonlinear, and Full Reynolds Stress Turbulence Models

*Khaled S. Abdol-Hamid*
*Langley Research Center, Hampton, Virginia*

National Aeronautics and
Space Administration

Langley Research Center
Hampton, Virginia 23681-2199

April 2018

The use of trademarks or names of manufacturers in this report is for accurate reporting and does not constitute an official endorsement, either expressed or implied, of such products or manufacturers by the National Aeronautics and Space Administration.

Available from:

NASA STI Program / Mail Stop 148
NASA Langley Research Center
Hampton, VA 23681-2199
Fax: 757-864-6500

# Abstract

The development and implementation of kL-based Reynolds Average Navier-Stokes (RANS) turbulence models are reported herein. The kL is based on Abdol-Hamid's closure and Menter's modification to Rotta's two-equation model. Rotta shows that a reliable transport equation can be formed from the turbulent length scale L, and the turbulent kinetic energy k. Rotta's kL equation is well suited for term-by-term modeling and displays useful features compared to other scale formulation. One of the important differences is the inclusion of higher order velocity derivatives in the source terms of the scale equation. This can enhance the ability of RANS solvers to simulate unsteady flows in URANS mode. The present report documents the formulation of three model levels of turbulence models as implemented in the CFD code FUN3D. Methodology and calibration examples are shown in detail. The levels are the linear k-kL and the two-equation algebraic Reynolds stress model (ARSM) as well as the full Reynolds Stress Model (RSM). Attached, separated and corner flow cases are documented and compared with experimental, theoretical and other turbulence model data. The results show generally very good comparisons with canonical and experimental data. The results from this formulation are similar or better than results using the SST two-equation turbulence model. ARSM shows great promise with similar level of computational resources as general two equation turbulence models.

# Nomenclature

| | |
|---|---|
| $C_d$ | drag coefficient |
| $\mathcal{H}$ | Heaviside function |
| L | turbulent length scale |
| $L_{vk}$ | von Kármán length scale |
| M | Mach number |
| $M_t$ | turbulent Mach number, $\sqrt{2k/a^2}$ |
| N | number of nodes in grid |
| $P_k$ | production of turbulent kinetic energy |
| $P_{kL}$ | production of turbulent kL |
| Re | Reynolds number |
| $R_{ij}$ | Reynolds stress components |
| $Re_L$ | Reynolds number based on length L |
| $Re_\theta$ | Reynolds number based on momentum thickness |
| $Re_x$ | local Reynolds number |
| $\boldsymbol{S}$, $S_{ij}$ | symmetric strain rate tensor |
| $\vec{U}, u_i$ | Cartesian velocity vector, $(u, v, w)^T$ |
| $\boldsymbol{W}$, $W_{ij}$ | asymmetric vorticity rate tensor |
| a | local speed of sound |
| b | half width of stream, where $(u - u_e)$ is half of $(u_m - u_e)$ |
| c | chord |
| $c_f$ | local skin friction coefficient |
| d | distance normal to surface |
| $f_2$ | blending function for model corrections |

| | |
|---|---|
| $f_c$ | auxiliary function in compressibility model |
| $f_{(kL)}$ | auxiliary function in (kL) transport equation |
| h | grid spacing measure |
| k | turbulent kinetic energy |
| p | pressure |
| r | radius |
| T | temperature |
| t | time |
| $u_e$ | edge velocity of outer co-flowing jet stream |
| $u_m$ | peak velocity of co-flowing jet stream |
| $u^+$ | velocity in wall units |
| $x_i$ | Cartesian coordinates, $(x, y, z)$ |
| $y^+$ | distance normal to surface in wall units |
| acoustic | based on ambient conditions |
| exit | relating to exit conditions |
| $\infty$ | freestream condition |
| jet | relating to jet conditions |
| max | maximum |
| min | minimum |
| splitter | splitter plate in planar co-flowing jet case |
| t | total condition |
| 2D | two-dimensional |
| 3D | three-dimensional |
| ARSM | algebraic Reynolds stress model |
| ARN | acoustic research nozzle |
| CFD | Computational Fluid Dynamics |
| C-D | convergent-divergent |
| DNS | direct numerical simulation |
| LES | large eddy simulation |
| NPR | nozzle pressure ratio, $p_{t,jet}/p_\infty$ |
| NTR | nozzle temperature ratio, $T_{t,jet}/T_\infty$ |
| RANS | Reynolds averaged Navier-Stokes |
| RSM | Reynolds stress model |
| SAS | scale-adaptive simulation |
| SST | shear stress transport |
| URANS | unsteady Reynolds averaged Navier-Stokes |
| $\delta_{ij}$ | Kronecker delta |
| $\varepsilon$ | scalar dissipation |
| $\theta$ | momentum thickness |
| $\kappa$ | von Kármán constant |
| $\mu$ | bulk viscosity |
| $\mu_t$ | turbulent eddy viscosity |
| $\omega$ | specific dissipation rate |
| $\Pi_{ij}$ | pressure strain |

| | |
|---|---|
| $\rho$ | density |
| $\tau_{ij}$ | Reynolds stress tensor |
| $'$ | first derivative |
| $''$ | second derivative |

# 1 Introduction

THE mechanism of the scale equation for determining turbulent length scale is not fully understood and most formulations use a special boundary condition to simulate its wall boundary condition. Even the more complex model closures like Reynolds stress models (RSM) or explicit algebraic Reynolds stress models (ARSM) still use a scale equation. Almost all two-equation models use the turbulent kinetic energy, k, and its transport equation as one of the primary variables.

Historically, the modeling of the scale equation using dimensional arguments has been purely heuristic [1]. Many of the linear two-equation models for the production use strain-rate or vorticity derived from the mean flow terms, resulting in only one scale from the equilibrium of source terms for both equations. The scale equation is considered, in most cases, the weakest link in turbulence models, including much more complex approaches such as differential Reynolds stress and hybrid RANS/LES (Reyolds Averaged Navier Stokes / Large Eddy Simulations) formulations. It is difficult to justify using any of the complex turbulence models without fixing or using an alternate form for the scale transport equation. One of the few exceptions is the modeling concept proposed by Rotta [2], which can be formed as an exact transport equation for the turbulent length scale, L. Rotta's approach is well suited for term-by-term modeling and displays very favorable characteristics, as compared to other approaches. A key difference is the inclusion of higher-order velocity derivatives in the source terms of the scale equation. This potentially allows for resolution of the turbulent spectrum in unsteady flows.

Menter et al. [3–5] presented a complete detailed form of the k-$\sqrt{\text{k}}$L two-equation turbulence model based on the Rotta [2] approach. In Menter, it was proposed to replace the problematic third derivative of the velocity, that occurred in Rotta's original model, with second derivatives of the velocity. Menter utilized this two-equation turbulence model to formulate the Scale-Adaptive Simulation (SAS) term that can be added to other two-equation models, such as Menter's shear stress transport (SST) [6]. The SAS concept is based on the introduction of the von Kármán length scale into the turbulence scale equation. The information provided by the von Kármán length scale allows SAS models to dynamically adjust to resolved structures in unsteady RANS (URANS) simulations. This can create LES-like behavior in unsteady regions of flow fields. At the same time, the model provides standard RANS capabilities in stable flow regions.

Abdol-Hamid [7] documented an initial form of the k-kL two-equation turbulence model. He showed the process to calibrate the constants within the range suggested by Rotta [2] and satisfying the near-wall logarithmic requirements. It naturally contains the SAS characteristics through the von Kármán length scale. The basic model was implemented in the computational fluid dynamics (CFD) code Propulsion Aerodynamics Branch 3-Dimensional (PAB3D) [8]. A recent modification to the basic model referred to as k-kL-MEAH2015 turbulence model is documented in reference 9. The k-kL-MEAH2015 model has been implemented in the fully unstructured Navier-Stokes 3-Dimensional (FUN3D) code in a loosely coupled manner. For brevity we will refer to k-kL-MEAH2015 as k-kL, herein. The implementation of k-kL in both CFL3D and FUN3D was verified in reference 9. Through private communication with researchers, Deutsches Zentrum fur Luft- und Raumfahrt e.V. (DLR)

independently verified k-kL in its TAU CFD code. In reference 9, the results were compared with theory and experimental data, as well as with results using the SST turbulence model. The k-kL model was shown to produce results similar or better than SST results. For example, for a separated axisymmetric transonic bump validation case, the size of the separation bubble (separation and reattachment locations) is better predicted by the k-kL model. Simulations have been carried out using five grid levels for the verification cases, avoiding grid refinement uncertainties. The validation results are compared with available experimental and/or theoretical data, depending upon the case. Most of the cases are taken from the turbulence modeling resource website [10, 11].

Subsonic and supersonic jet flows are quite difficult to predict with most RANS turbulence models. For subsonic jets, most turbulence models incorrectly predict the mixing rate so that the jet core length differs significantly from what is physically observed. The k-kL model also predicts a core length that is too short. A proposed jet correction, including compressibility effects, is described and is designated k-kL+J. It is also well known that most two-equation turbulence models under-predict mixing in the shear layer for high-temperature jet flow. A proposed jet plus temperature correction is presented and designated as k-kL+J+T. A set of cases are selected to calibrate the model for different flow characteristics. A flat plate case is used to calibrate the model's main constants for attached flow and maintain the range of constant values within recommended values. The axisymmetric transonic bump is used as the standard case for separated flow. Subsonic, high-speed and high-temperature cases are selected to calibrate the model for jet flow cases.

In the present report, we document the kL length-scale through the k-kL formulation and the process to calibrate and implement it in CFD solvers. Theories for higher-order turbulence models such as RSM have been around for some time. The Launder Reece Rodi (LRR) [12] and Speziale Sarker Gatski (SSG) [13] are among the well known pressure-strain models. Hanjalic [14] provides a summary of different RSM. These models require much larger resources than two-equation turbulence models by adding five more equations. Other efforts are made to develop the Alegbriac Reynols Stress Moodel (ARSM) based on SSG [13] that would require similar resources as general two-equation turbulence models. We will use the ARSM model that is fully documented and tested by Rumsey and Gatski [15] and Girimaji [16]. Another type of nonlinear model is introduced by Spalart [17] known as the Quadratic Constitutive Relation (QCR). These models have only had a minor additional impact to the overall computational effort and have the potential to resolve some of the errors and poor capabilities of linear turbulence models. The present paper documents the formulations of RSM and ARSM based on kL formuation. These models are compared with linear k-kL, other turbulence models, theoretical and experimental data that covers a wide range of flow complexitity [18–25]. In general, ARSM shows the most promising results out of all the models presented here.

# 2 Computational Methods

FUN3D is an unstructured three-dimensional, implicit, Navier-Stokes code. Roe's flux difference splitting [26] construction schemes include HLLC [27], AUFS [28], and LDFSS [29]. The default method for calculation of the Jacobians is the flux function of van Leer [30], but the method by Roe and the Harten-Lax-van Leer-Contact (HLLC) scheme, artificially upstream flux vector splitting (AUFS) scheme, and Edwards' low diffusion flux splitting scheme (LDFSS) are also available. The use of flux limiters are mesh- and flow-dependent. Flux limiting options include MinMod [31] and methods by Barth and Jespersen [32] and Venkatakrishnan [33]. Other details regarding FUN3D can be found in Anderson and Bonhaus [34] and Anderson et al. [35], as well as in the extensive bibliography that is accessible at the FUN3D web site, http://fun3d.larc.nasa.gov.

# 3 Turbulence Models Description

The kL length scale formulation is the base of the turbulence models presented in this section. The baseline k-kL turbulence model is described in section 3.1. The two-equation nonlinear ARSM based on kL is documented in section 3.2. The seven-equation turbulence model formulation of RSM is documented in section 3.3. Models to correct for free shear flows and compressibility effects are described in section 3.4.1. This correction could be used for all turbulence levels. High-temperature shear flow correction is described in section 3.4.2. This correction is currently limited to only two-equation turbulence models.

## 3.1 Baseline two-equation k-kL Model

The k-kL two-equation turbulence model, equations 1 through 11, is based on Rotta's k-kL approach with the modifications proposed by Menter [3–5] to develop a k-$\sqrt{\text{k}}$L model. A complete list of coefficients used by the present model is defined. where the third derivative of velocity was replaced with the second derivative of velocity. The closure constants were derived and documented by Abdol-Hamid [9].

$$\frac{\partial \rho k}{\partial t} + \frac{\partial \rho u_j k}{\partial x_j} = P_k + \frac{\partial}{\partial x_j}\left(\left(\mu_l + \sigma_{(k)}\mu_t\right)\frac{\partial \rho k}{\partial x_j}\right) - C_w \mu_l \frac{k}{d^2} - C_k \rho \frac{k^{2.5}}{kL} \tag{1}$$

$$\frac{\partial \rho kL}{\partial t} + \frac{\partial \rho u_j kL}{\partial x_j} = \left[\mathrm{C}_{(kL)_1}\frac{kL}{k}P_{kL} + \frac{\partial}{\partial x_j}\left(\left(\mu_l + \sigma_{(kL)}\mu_t\right)\frac{\partial \rho kL}{\partial x_j}\right) - 6\mu_l \frac{kL}{d^2} f_{(kL)}\right]$$

$$-\mathrm{C}_{(kL)_2}\rho k^{1.5} \tag{2}$$

The production of turbulent kinetic energy is stress-based (eq. 3). and is limited in both the k and kL equations (eq. 5).

$$\mathrm{P} \;=\; \tau_{ij}\frac{\partial u_i}{\partial x_j} \tag{3}$$

The linear approach (L), for which stress is directly proportional to strain is as follows:

$$\tau_{ij} = \tau_{ij}^{(L)} = 2\mu_\mathrm{t}\left(\mathrm{S}_{ij} - \frac{1}{3}tr\{\boldsymbol{S}\}\delta_{ij}\right) - \frac{2}{3}\rho \mathrm{k}\delta_{ij} \tag{4}$$

$$\mathrm{S}_{ij} = \frac{1}{2}\left(\frac{\partial u_i}{\partial x_j} + \frac{\partial u_j}{\partial x_i}\right), W_{ij} = \frac{1}{2}\left(\frac{\partial u_i}{\partial x_j} - \frac{\partial u_j}{\partial x_i}\right)$$

$$P = \mu_t S^2 = 2\mu_t S_{ij} S_{ij}$$

$$\mathrm{P}_{kL} = \mathrm{P}_\mathrm{k} \;=\; \min\left(\mathrm{P}, 20\,\mathrm{C}_\mu{}^{3/4}\frac{\rho \mathrm{k}^{5/2}}{kL}\right) \tag{5}$$

with the turbulent eddy viscosity computed using equation 6.

$$\mu_t = \frac{C_\mu^*}{C_\mu} C_\mu^{1/4}\frac{\rho kL}{k^{1/2}} \tag{6}$$

For the linear approach, $C_\mu^*$ equals $C_\mu$. The nonlinear ARSM model computes this coefficient as described in section 3.2. The functions and coefficients are

$$\begin{aligned}
\mathrm{C_k} &= {\mathrm{C}_\mu}^{3/4}, \quad {\mathrm{C}_{(kL)}}_1 = \zeta_1 - \zeta_2 A_L^2, \quad A_L = \left(\frac{kL}{\mathrm{kL}_{vk}}\right), \quad {\mathrm{C}_{(kL)}}_2 = \zeta_3 \\
f_{(kL)} &= \frac{1 + \mathrm{C}_{d1}\xi}{1 + \xi^4}, \quad \xi = \frac{\rho\sqrt{0.3\mathrm{k}}\mathrm{d}}{20\mu} \\
\mathrm{L}_{vk} &= \kappa \left| \frac{\mathrm{U}'}{\mathrm{U}''} \right|, \quad \mathrm{U}' = \sqrt{2\mathrm{S}_{ij}\mathrm{S}_{ij}}, \quad \mathrm{U}'' = \sqrt{\frac{\partial^2 \mathrm{u}_i}{\partial x_k^2}\frac{\partial^2 \mathrm{u}_i}{\partial x_j^2}}
\end{aligned}$$

The second derivative expression of the velocity can be written out as:

$$\mathrm{U}'' = \sqrt{\left(\frac{\partial^2 u}{\partial x^2} + \frac{\partial^2 u}{\partial y^2} + \frac{\partial^2 u}{\partial z^2}\right)^2 + \left(\frac{\partial^2 v}{\partial x^2} + \frac{\partial^2 v}{\partial y^2} + \frac{\partial^2 v}{\partial z^2}\right)^2 + \left(\frac{\partial^2 w}{\partial x^2} + \frac{\partial^2 w}{\partial y^2} + \frac{\partial^2 w}{\partial z^2}\right)^2} \tag{7}$$

The effective production of the kL equation is defined as

$$P_{kL}(eff) = C_{(kL)_1}\frac{(kL)}{k}P_{kL} \tag{8}$$

where,

$$C_{(kL)_1} = \zeta_1 - \zeta_2 A_L^2, \; A_L = \frac{L}{L_{vk}}$$

The standalone $\mathrm{L}_{vk}$ has singularity as $\mathrm{U}'$ and $\mathrm{U}''$ approach zero. Likely, $\mathrm{L}_{vk}$ is part of $P_{kL}(eff)$ and $A_L$ terms of equation 8.

$$if \; (\mathrm{U}'' = 0 \; and \; \mathrm{U}' = 0), \; P_{kL}(eff) = 0 \tag{9}$$

For all other conditions, following Menter et al. [3–5] with correction proposed by Abdol-Hamid [7] for separated flow, we apply this limit on $\mathrm{L}_{vk}$,

$$if \; \mathrm{U}'' > 0 \; and \; \mathrm{U}' \geq 0)$$

$$\begin{aligned}
\mathrm{L}_{vk,\min} \leq \mathrm{L}_{vk} \leq \mathrm{L}_{vk,\max}, \quad \mathrm{L}_{vk,\min} &= \frac{kL}{\mathrm{kC}_{11}}, \quad \mathrm{L}_{vk,\max} = \mathrm{C}_{12}\kappa\mathrm{d}f_\mathrm{p} \\
f_\mathrm{p} &= min\left[max\left(\frac{\mathrm{P_k}kL}{\mathrm{C}^{3/4}\rho\mathrm{k}^{5/2}}, \mathrm{C}_{13}\right), 1.0\right]
\end{aligned} \tag{10}$$

The boundary conditions for the two turbulence variables, k and kL, along solid walls and the recommended farfield boundary conditions for most applications are

$$\mathrm{k_{wall}} = (\mathrm{kL})_{\mathrm{wall}} = 0, \quad \mathrm{k}_\infty = 9 \times 10^{-9}\mathrm{a}_\infty^2, \quad (\mathrm{kL})_\infty = 1.5589 \times 10^{-6}\frac{\mu_\infty \mathrm{a}_\infty}{\rho_\infty} \tag{11}$$

where $a_\infty$ represents the speed of sound. The constants are:

$$\begin{aligned}
\sigma_\mathrm{k} &= 1.0, \quad \sigma_{(\mathrm{kL})} = 1.0 \\
\kappa &= 0.41, \quad \mathrm{C}_\mu = 0.09 \\
\zeta_1 &= 1.2, \quad \zeta_2 = 0.97, \quad \zeta_3 = 0.13 \\
\mathrm{C}_{11} &= 10.0, \quad \mathrm{C}_{12} = 1.3, \quad \mathrm{C}_{13} = 0.5, \quad \mathrm{C}_{\mathrm{d1}} = 4.7, \quad \mathrm{C_w} = 2.0
\end{aligned}$$

### 3.2 Nonlinear two-equation k-kL Model

Little data exist for implementing explicit ARSM using a generalized three-dimensional Navier-Stokes method such as FUN3D. One approach is to develop algebraic relations with the tensors $T^{(\lambda)}$ as

$$\tau_{ij} = \tau_{ij}^{(ARSM)} = -\rho k \left[ a_{ij} + \frac{2}{3}\delta_{ij} \right] = -\rho k \left[ \sum \beta_\lambda T^{(\lambda)} + \frac{2}{3}\delta_{ij} \right] \tag{12}$$

These tensors are function of strain, $S$, and vorticity, $W$, rates. Reference 36 shows the most general representation for a symmetric traceless second-order tensor, such as $a_{ij}$, which depends on two other second-order tensors, is a tensor polynomial containing ten tensorially independent groups, $T^{(\lambda)}$:

$$\begin{array}{l} T^{(1)} = \left[ S^* - \frac{1}{3} tr\left\{S^*\right\} \right],\ T^{(2)} = \left[ S^{*2} - \frac{1}{3} tr\left\{S^{*2}\right\} \right] \\ T^{(3)} = \left[ W^{*2} - \frac{1}{3} tr\left\{W^{*2}\right\} \right],\ T^{(4)} = \left[ S^* W^* - W^* S^* \right] \\ T^{(5)} = \left[ S^{*2} W^* - W^* S^{*2} \right],\ T^{(6)} = \left[ S^* W^{*2} - W^{*2} S^* - \frac{2}{3} tr\left\{S^* W^{*2}\right\} \right] \\ T^{(7)} = \left[ S^{*2} W^{*2} + W^{*2} S^{*2} - \frac{2}{3} tr\left\{S^{*2} W^{*2^*}\right\} \right],\ T^{(8)} = \left[ W^* S^* W^{*2} - W^{*2} S^* W^* \right] \\ T^{(9)} = \left[ W^* S^* W^{*2} - W^{*2} S^* W^* \right],\ T^{(10)} = \left[ W^* S^{*2} W^{*2} - W^{*2} S^{2*} W^* \right] \end{array}$$

For example, Wallin [36] described an ARSM that uses five tensors, ($\lambda$ = 1, 3, 4, 6, and 9), that is based on the LRR turbulence pressure-strain model [12]. In the present report, we will focus on the cubic-based model from refernces [15] and [16] that are based on SSG [13]. We will refer to this model as k-kL-ARSM. This ARSM utilizes three tensors ($\lambda$ = 1, 2, and 4) as follows:

$$\tau_{ij}^{(ARSM)} = -\rho k \left( \beta_1\, T^{(1)} + \beta_2\, T^{(2)} + \beta_4\, T^{(4)} + \frac{2}{3}\delta_{ij} \right) \tag{13}$$

$T^{(1)}$ is the linear part of the model. However, $T^{(2)}$, and $T^{(4)}$ are the nonlinear terms that model the anisotropy. The coefficients for these terms are

$$\beta_1 = -2C_\mu^* = 2\alpha,\ \beta_2 = 2a_4 a_3 \beta_1,\ \beta_4 = -a_4 a_2 \beta_1 \tag{14}$$

In this model, $C_\mu^*$ is limited to be no smaller than 0.0005. For cubic based ARSM, $\alpha$ is the root of the cubic equation

$$\alpha^3 + p\alpha^2 + q\alpha + r = 0 \tag{15}$$

where coefficients in equation 14 are defined as:

$$\begin{array}{c} a_1 = \frac{1}{2}\left( \frac{4}{3} - C_2 \right),\ a_2 = \frac{1}{2}\left(2 - C_4\right) \\ a_3 = \frac{1}{2}\left(2 - C_3\right),\ a_4 = \tau\left[\gamma_1^* - 2\alpha\gamma_0^*\eta^2\tau^2\right]^{-1} \end{array} \tag{16}$$

We also use the following definitions and constants.

$$\tau = \frac{C_\mu^{1/4}}{C_\mu}\frac{(kL)}{k^{3/2}},\ W_{ij}^* = \tau W_{ij},\ S_{ij}^* = \tau S_{ij}$$

$$\eta^2 = \left\{S^{*2}\right\},\ \gamma_0^* = \frac{C_1^1}{2}, \gamma_1^* = \frac{C_1^0}{2} + \left( \frac{C_{\varepsilon 2} - C_{\varepsilon 1}}{C_{\varepsilon 1} - 1} \right)$$

$C_{\varepsilon 1} = 1.44,\ C_{\varepsilon 2} = 1.83$
$C_1^1 = 1.8,\ C_1^0 = 3.4$
$C_2 = 0.36,\ C_3 = 1.25,\ C_4 = 0.6$

$$p = -\frac{\gamma_1^*}{\eta^2 \gamma_0^*}$$

$$q = \frac{1}{\left(2\eta^2\gamma_0^*\right)^2}\left(\gamma_1^{*2} - 2\eta^2\gamma_0^* a_1 - \frac{2}{3}\eta^2 a_3^2 - 2R^2\eta^2 a_2^2\right)$$

$$r = \frac{\gamma_1^* a_1}{\left(2\eta^2\gamma_0^*\right)^2}$$

$$\left\{W^{*2}\right\} = -W_{ij}^* W_{ij}^*,\ R^2 = -\frac{\left\{W^{*2}\right\}}{\left\{S^{*2}\right\}}$$

The correct root to choose from this cubic equation is the root with the lowest real part. $\eta^2 < 10^{-6}$

$$\alpha = -\frac{\gamma_1^* a_1}{\gamma_1^{*2} - 2\left\{W^{*2}\right\} a_2^2}$$

Otherwise, define:

$$a = q - \frac{p^2}{3},\ b = \frac{1}{27}\left(2p^3 - 9pq + 27r\right),\ d = \frac{b^2}{4} + \frac{a^3}{27}$$

if d $> 0$ then

$$t_1 = \left(-\frac{b}{2} + \sqrt{d}\right)^{1/3},\ t_2 = \left(-\frac{b}{2} - \sqrt{d}\right)^{1/3}$$

$$\alpha = \min\left(-\frac{p}{3} + t_1 + t_2, -\frac{p}{3} - \frac{t_1}{2} - \frac{t_2}{2}\right)$$

else if d $\leq 0$

$$\theta = \cos^{-1}\left(-\frac{b}{2\sqrt{\frac{a^3}{27}}}\right)$$

$$t_1 = -\frac{p}{3} + 2\sqrt{-\frac{a}{3}}\cos\left(\frac{\theta}{3}\right),\ t_2 = -\frac{p}{3} + 2\sqrt{-\frac{a}{3}}\cos\left(\frac{2\pi}{3} + \frac{\theta}{3}\right),\ t_3 = -\frac{p}{3} + 2\sqrt{-\frac{a}{3}}\cos\left(\frac{4\pi}{3} + \frac{\theta}{3}\right)$$

$$\alpha = \min\left(t_1, t_2, t_3\right)$$

For the nonlinear two-equation turbulence models, $C_{13}$, in equation 10, is set to 0.25 and $C_w$, in equation 1, is set to 1.5. Also, the production term for $kL$, $P_{kL}$, is limited by production based on strain rate, $S$ and linear turbulence viscosity ($\mu_t^L$), as follows:

$$P_k = \tau_{ij}\frac{\partial u_i}{\partial x_j}, \quad P_{kL} = \max(P_k, \mu_t^L S^2), \quad \mu_t^L = C_\mu^{1/4}\frac{\rho(kL)}{k^{1/2}} \tag{17}$$

The original SSG model had a value of 0.8 for $a_2$ in equation 16. In the present kL-based model, $a_2$ of 0.7 is calibrated to improve the results for the 2D NASA Hump (see section 4.5). The change in $a_2$ is within recommended values (0.5-0.85). This change and limiting kL production improves the results for all separated flow cases discussed in sections 4.5, 4.6, and 4.7.

Another form of ARSM is introduced by Spalart [17] known as the Quadratic Constitutive Relation. We will refer to this model as k-kL-QCR. Instead of the traditional linear Boussinesq relation, the following form for the turbulent stress is used:

$$\tau_{ij}^{(ARSM)} = \tau_{ij} - C_{cr1}(Q_{ik}\tau_{jk} + Q_{jk}\tau_{ik}) = -\rho k\left[\beta_1 T^{(1)} + \beta_4 T^{(4)} + \frac{2}{3}\delta_{ij}\right] \tag{18}$$

$$Q_{ik} = \frac{2W_{ik}}{\sqrt{\frac{\partial u_m}{\partial x_n}\frac{\partial u_m}{\partial x_n}}}.\ \beta_1 = -2 * 0.09,\ \beta_4 = \frac{2\beta_1 C_{cr1}}{\tau\sqrt{\frac{\partial u_m}{\partial x_n}\frac{\partial u_m}{\partial x_n}}} \tag{19}$$

Where, $Q_{ik}$ is an antisymmetric normalized rotation tensor.

### 3.3 Full Reynolds Stress Model (RSM)

The RSMs solve transport equations for each of the six Reynolds stresses, $R_{ij}$, as follows:

$$\frac{\partial \rho R_{ij}}{\partial t} + \frac{\partial \rho u_k R_{ij}}{\partial x_k} = \left[P_{ij} + \Pi_{ij} + \frac{\partial}{\partial x_j}\left(\left(\mu_l + D\frac{k^2}{\varepsilon}\right)\frac{\partial \rho R_{ij}}{\partial x_k}\right)\right] - C_k\rho\frac{2k^{2.5}}{3kL}\delta_{ij} \tag{20}$$

A seventh equation is required to determine the length scale variable, in this case $kL$. The relation between stress components and production is defined as:

$$\rho R_{ij} = -\tau_{ij},\ P_{ij} = -\rho\left(R_{ik}\frac{\partial u_j}{\partial x_k} + R_{jk}\frac{\partial u_i}{\partial x_k}\right)$$
$$P_k = \frac{1}{2}P_{ii},\ k = \frac{1}{2}R_{ii},\ P_{kL} = \max(P_k, \mu_t S^2)$$

The pressure-strain model is defined in reference [14] as:

$$\Pi_{ij} = \Pi_{ij,1} + \Pi_{ij,2}$$

The aniosotropy tensor is defined as:

$$a_{ij} = \left(\frac{R_{ij}}{k} - \frac{2}{3}\delta_{ij}\right)$$
$$A_2 = a_{pq}a_{qp},\ A_3 = a_{pq}a_{qr}a_{rp},\ A = 1 - \frac{9}{8}(A_2 - A_3),\ AS = a_{pq}S_{qp}$$

The slow term:

$$\Pi_{ij,1} = -\varepsilon\left[C_1 a_{ij} + C_2(a_{ip}a_{pj} - \frac{1}{3}A_2\delta_{ij})\right] \tag{21}$$

The rapid term: may contain free, linear, quadratic and cubic components:

$$\begin{aligned}
\Pi_{ij,2} = &\left(C_3 - C_3^*\sqrt{A_2}\right)kS_{ij} && free(S)\\
&+C_4(a_{ip}S_{pj} + S_{ip}a_{pj} - \frac{2}{3}a_{pq}S_{pq}\delta_{ij})k && linear(S)\\
&+C_5(W_{ip}a_{pj} - a_{ip}W_{pj})k && linear(W)\\
&+C_1^* P_k a_{ij} && quadratic\\
&+C_6\left[a_{ip}a_{pq}S_{qj} + S_{ip}a_{pq}a_{qj} - 2a_{ip}S_{pq}a_{qj} - 3A_2 S_{ij}\right]k && quadratic(S)\\
&+C_7\left[W_{ip}a_{pq}a_{qj} - a_{ip}a_{pq}W_{qj}\right]k && quadratic(W)\\
&+C_8\left[a_{pq}^2(W_{ip}a_{pj} - a_{ip}W_{pj}) + \frac{3}{2}(a_{ip}W_{pq}a_{qr}a_{rj} - a_{ip}a_{pq}W_{qr}a_{rj}\right]k && cubic(W)
\end{aligned} \tag{22}$$

Similar to ARSM, $C_{13}$, in equation 10, is set to 0.25 and the production for kL equation is limited by the linear production, $\mu_t S^2$.

$$P_k = \tau_{ij}\frac{\partial u_i}{\partial x_j}, P_{kL} = \max(P_k, \mu_t S^2) \tag{23}$$

Table 1 lists the coefficients for pressure-strain terms for LRR [12], SSG [13], and LRR with Cubic (LRR+C) terms. The pressure-strain term for LRR is considered linear with the anisotropy tensor, $a_{ij}$. The SSG is quadratic in the pressure-strain terms due to $P_k$ $a_{ij}$ term. The LRR+C is a cubic-based formulation in the pressure-strain terms. We also testing a mix between SSG and LRR (SSG-LRR-kL). Using this approach, LRR is used close to the wall, and SSG is used in the wake region or far from the wall.

$$C_n = f_2 C_n^{LRR} + (1 - f_2) C_n^{SSG} \tag{24}$$

The blending function, $f_2$, is similar to the one used by SST to switch between k-$\omega$ and k-$\varepsilon$. This modification does not affect attached flow simulations and is active only in the wake or shear flow regions:

$$f_2 \;=\; tanh\left(\Gamma^2\right), \quad \Gamma = max\left(2\frac{\sqrt{\mathrm{k}}}{\mathrm{C}_\mu \omega \mathrm{d}}, \frac{500\nu}{\mathrm{d}^2\omega}\right), \quad \omega = \frac{\mathrm{k}^{3/2}}{kLC_\mu^{1/4}} \tag{25}$$

We are not in any way recommending the RSM for large-scale aerodynamic problems such as a database that requires thousands of CFD simulations. The RSM is mainly used as a learning tool, the results of which may improve the capabilities of ARSM. For example, the effect of limiting $P_{kL}$ and its effect on improving shear stress results was first observed using RSM and successfully applied to ARSM. To keep the documentation short, we will only show sample results for the full Reynolds stress models. So, the focus will be more for attached, separated, and crossflow cases. In general, we are using RSM-kL as general label for all RSM for the cases with similar results and results from using the SSG pressure-strain model. For the results that show significant difference, we will refer to each model as labeled in this section.

Table 1. Summary of coefficients in pressure-strain models.

| Model | $C_1$ | $C_1^*$ | $C_2$ | $C_3$ | $C_3^*$ | $C_4$ | $C_5$ | $C_6$ | $C_7$ | $C_8$ |
|---|---|---|---|---|---|---|---|---|---|---|
| LRR | 1.8 | 0.0 | 0.0 | 0.8 | 0.0 | 0.97 | 0.578 | 0.0 | 0.0 | 0.0 |
| SSG | 1.7 | 0.9 | -1.05 | 0.8 | 0.65 | 0.625 | 0.20 | 0.0 | 0.0 | 0.0 |
| LRR+C | 1.8 | 0.0 | 0.0 | 0.8 | 0.0 | 0.97 | 0.578 | 0.0 | 0.2 | 0.2 |

## 3.4 Corrections to Model

### 3.4.1 Jet Corrections for Free Shear and Compressibility, +J

Subsonic and supersonic jet flows are quite difficult to predict with most RANS turbulence models. For subsonic jets, turbulence models do not predict the correct mixing rate and either predict core lengths that are too short or too long. The base k-kL model also predicts a too short core length.

However, it turns out that the k-kL model also predicts the correct mixing rate and shorter core length. By modifying the diffusion coefficient of the k-equation, the mixing rate is improved, using the following equation.

$$\sigma_{\mathrm{k}} \;=\; f_2\sigma_{\mathrm{k}_1} + (1 - f_2)\,\sigma_{\mathrm{k}_2}, \quad \sigma_{\mathrm{k}_1} = 1.0, \quad \sigma_{\mathrm{k}_2} = 0.5, \tag{26}$$

From our early investigations, linear k-kL produces excellent results for jet cases, whereas ARSM degrades the results. To avoid this problem, we use the same blending function to activate the linear stress and mask the ARSM values when used as follows:

$$\tau_{ij} = f_2 \tau_{ij}^{(ARSM)} + (1 - f_2)\, \tau_{ij}^{(L)} \tag{27}$$

Most turbulence models fail to predict high-speed shear flow, as the mixing is much slower than subsonic flow. A compressibility correction is the approach used by most turbulence models to improve this deficiency. We propose to use an approach similar to Wilcox's compressibility with cut-off Mach number to activate the compressibility for supersonic flow and not affect subsonic shear flow, as listed in equations 28 and 29.

$$\mathrm{C_k} \;=\; \mathrm{C_\mu^{3/4}}\,(1 + f_c)\,, \quad \mathrm{C}_{kL2} = \zeta_3 + 2.5\mathrm{C_\mu^{3/4}} f_c \tag{28}$$

$$f_c \;=\; 1.5(1.0 - f_2)\left(\mathrm{M_t^2} - \mathrm{M_0^2}\right)\mathcal{H}\left[\mathrm{M_t^2} - \mathrm{M_0^2}\right], \quad \mathrm{M_t} = \sqrt{\frac{2\mathrm{k}}{a^2}} \tag{29}$$

For linear turbulence model $\mathrm{M_0}$ is set to 0.17 and for nonlinear turbulence models $\mathrm{M_0}$ is set to 0.10.

### 3.4.2 Temperature Correction for High-Temperature Jet, +T

It is well known that most two-equation turbulence models under-predict mixing in the shear layer for high-temperature jet flows. Most models were developed and calibrated for room temperature, low Mach number, and plane mixing layer flows. For high-temperature jet flow, the standard turbulence models lack the ability to model the observed increase in growth rate of mixing layers [19]. We propose a correction similar to the approach introduced by Abdol-Hamid [7]. For k-kL turbulence models, we have calibrated the correction for one of the high-temperature jets from Bridges data [19], specifically Set Point 46. The correction is formulated as

$$f_\mu = \left[1 + 3.65 T_g^3\right] \tag{30}$$

$$T_g = |\nabla(T_t)| \frac{kL}{T_t k C_\mu^{0.75}} \tag{31}$$

Now, $\mu_t = f_\mu \rho C_\mu^{0.25} kL/k^{0.5}$. This temperature-corrected model is termed k-kL+T. When the model includes the free shear and compressibility correction terms as well as the temperature correction, it is termed k-kL+J+T.

# 4 Test Case Descriptions

The Transformational Tools and Technologies (TTT) Project has defined a Technical Challenge to identify and down-select turbulence model technologies for 40% reduction in predictive error against standard test cases for turbulent separated flows, free shear flows, and shock-boundary layer interactions. In addition to the standard zero pressure gradient flat plate, we have selected four cases to use in the calibration throughout the development of kL-based turbulence models, which are described in subsections 4.1 through 4.3. Table 2 lists relevant aspects of the simulation for each case. The flat plate is low-speed attached flow with little, if any, compressibility effects. The jet flows [19] display both low- and high-compressibility characteristics as well as high-temperature jet flow. The high-speed mixing layer [20] is to evaluate the compressibility correction for shear flow. The 2D wall-mounted hump [21] flow has both flow separation and reattachment points. This case is used to

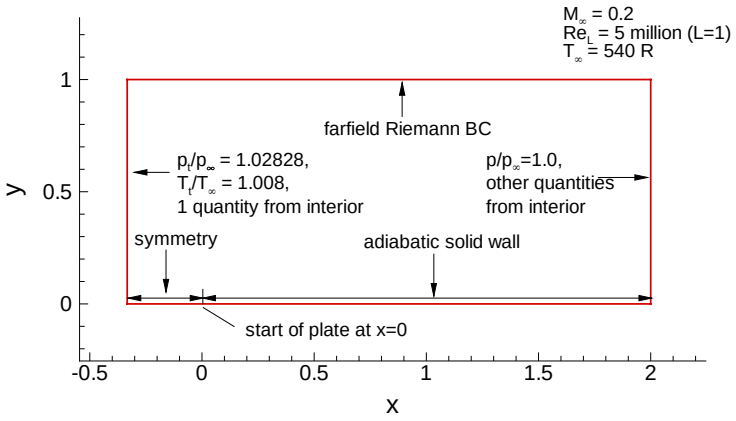


Figure 1. Flat plate geometry and boundary conditions.

calibrate both k-kL and k-kL-ARSM formations. The transonic bump and supersonic compression corner cases are used to validate the capabilities on the kL formulation in predicting separation and reattachment locations. In addition to TTT cases, a supersonic square duct case [25] is computed. In the supersonic square duct, a secondary flow structure develops perpendicular to the main flow and is mainly attributed to the turbulence anisotropy which is not simulated by linear (isotropic) models. Comparisons are made with historic, canonical data or experimental results where available. Detailed grid studies are completed by Abdol-Hamid et al. [9]. In the present documentation, only the medium grids are utilized unless otherwise stated.

Table 2. Test Cases.

| Geometry | Grid | Flow physics |
|---|---|---|
| Subsonic flat plate [18] | two-dimensional | wall bounded, attached |
| Subsonic jet [19] | axisymmetric | free shear, low speed |
| Transonic jet [19] | axisymmetric | free shear, compressible |
| Subsonic high-temperature jet [19] | axisymmetric | free shear, high-temperature |
| High-speed mixing layer [20] | two-dimensional | free shear, compressible |
| Subsonic wall-mounted hump [21] | two-dimensional | wall bounded, separated |
| Transonic bump [22] | axisymmetric | wall bounded, separated |
| Supersonic compression corner [23] and [24] | axisymmetric | wall bounded, separated |
| Supersonic square duct [25] | three-dimensional | corner and crossflow |

## 4.1 Zero Pressure Gradient Subsonic Flat Plate

Figure 1 shows a sketch of the flat plate test case with boundary conditions used in this analysis. This is a subsonic, $M_\infty = 0.2$ case at Re = 5 million per unit length. The medium grid size for this case, used in the present investigation, is 13,289 nodes. To generate the present set of constants for the present kL-based two-equation turbulence formulations, we take the following steps:

- Justify the logarithmic region requirements

$$\frac{dU}{dy} = \frac{u_\tau}{\kappa d},\ k = \frac{u_\tau^2}{C_\mu^{0.5}},\ L = \kappa d,\ v_t = u_\tau \kappa d$$

- Fix $\zeta_3 = 0.13$ and limit the range for $1.1 < \zeta_1 < 1.3$ and $0.95 < \zeta_2 < 1.0$ as suggested by Rotta [2]

- Calibrate both coefficients to fit the results for the flat plate case

$$\zeta_2 = \zeta_1 - \zeta_3 \frac{1}{C_\mu^{0.75}} + \frac{k^2}{C_\mu^{0.5}}$$

The optimal values for these constants are

$$\zeta_1 = 1.2, \quad \zeta_2 = 0.97, \quad \zeta_3 = 0.13$$

Figure 2(a) shows $u^+$ velocity with respect to $y^+$, as designed, matching well with Cole's theory [18]. Figure 2(b) shows typical turbulent stress components ($\tau_{11}$, $\tau_{22}$, $\tau_{33}$, and $\tau_{12}$) using linear RANS turbulence models. The normal components do not show any aniosotropy characteristics as all the values are almost identical. Next, we compare the variations of two-

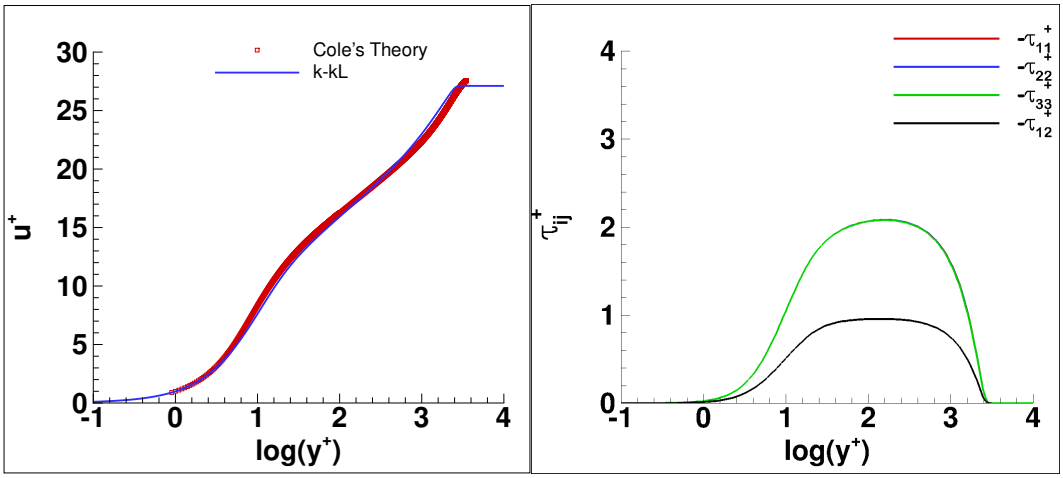


(a) Velocity profile, Cole's theory with different variation of kL turbulence models, $Re_\theta = 10{,}000$, Coles [18]; lines, FUN3D.

(b) Reynolds stress components.

Figure 2. Flat plate case, two-equation k-kL turbulence model results.

equation k-kL (linear, QCR, and ARSM) with well known linear turbulence models such as the SST. Figure 3(a) shows $u^+$ velocity with respect to $y^+$ using both linear and nonlinear RANS turbulence models compared with Cole's theory [18]. All models produced very similar results and compared well with the data. Figure 3(b) shows that the development of local skin friction varies with axial Reynolds number, $Re_x$. The results are plotted with Blasius's laminar boundary solution and the 1/5th power law for a turbulent boundary layer. k-kL and k-kL-QCR show smooth transitions from laminar to turbulent flow compared with SST results. There is no claim that k-kL is a transition model. The k-kL-ARSM shows overshoot in skin friction as it transitions from laminar to turbulent flow.

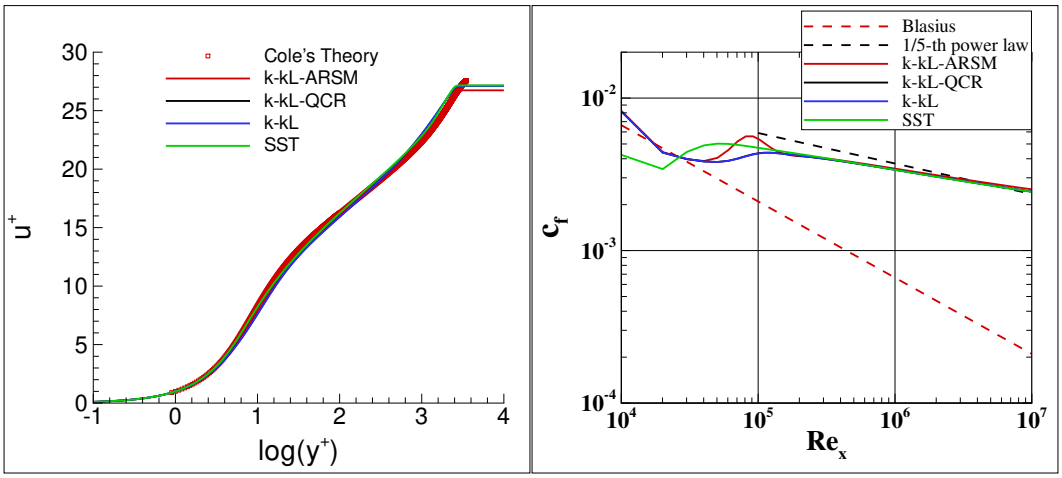


(a) Velocity profile, compared with Cole's theory, (b) Skin friction variations with Reynolds number. $Re_\theta$ = 10,000, Coles [18]; lines, FUN3D.

Figure 3. Flat plate case, two-equation turbulence model results.

Figure 4(a) shows $u^+$ velocity with respect to $y^+$ using the linear model, nonlinear (ARSM), and full RSM using SSG constants compared with Cole's theory [18]. All kL formulations produce very similar results and compared well with the data. Figure 4(b) shows the development of local skin friction with axial Reynolds number, $Re_x$. Both ARSM and RSM show overshoot in the skin friction as it transitions from laminar to turbulent flow, and they are very similar in value with RSM transitioning at lower $Re_x$.

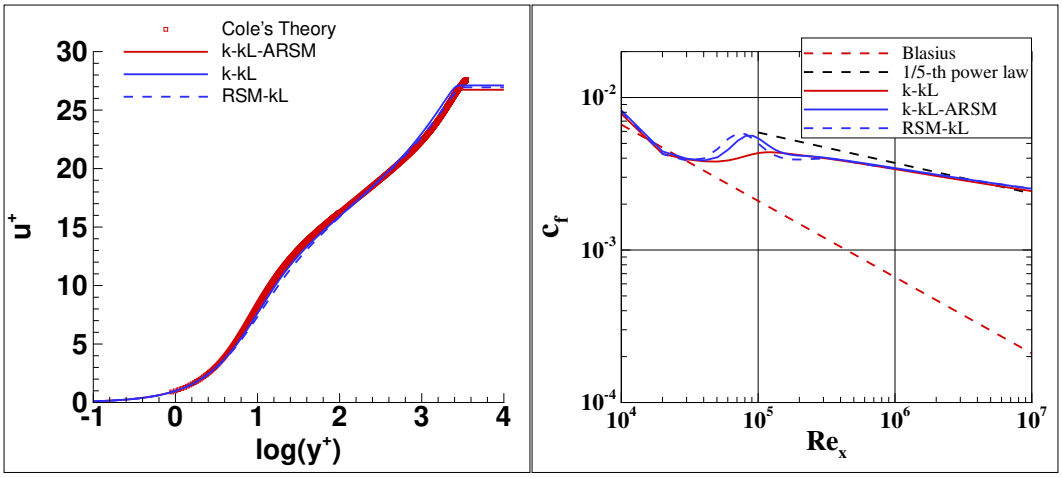


(a) Velocity profile, Cole's theory with different variation kL-based turbulence models, $Re_\theta$ = 10,000, Coles [18]; lines, FUN3D. (b) Skin friction variation with Reynolds number.

Figure 4. Flat plate case, kL-based turbulence model results.

Figure 5(a) shows typical turbulent stress components (streamwise $\tau_{11}$ top, wall-normal $\tau_{22}$ bottom, spanwise $\tau_{33}$ middle, and 2/3k for reference) with k-kL-ARSM. Figure 5(b) shows typical turbulent stress components ($\tau_{11}$, $\tau_{22}$, $\tau_{33}$. and 2/3k) SSG RSM-kL. Both

models show aniosotropy characteristics as all the values are different. The turbulent stress components produced by the ARSM and the RSM behave similarly. Similar to the Direct Numerical Simulation (DNS) [37] and Large Eddy Simulation (LES) [38], the $\tau_{22}$ and $\tau_{33}$ are packed together with the peak in $\tau_{11}$ further away. Figure 6 shows the results using

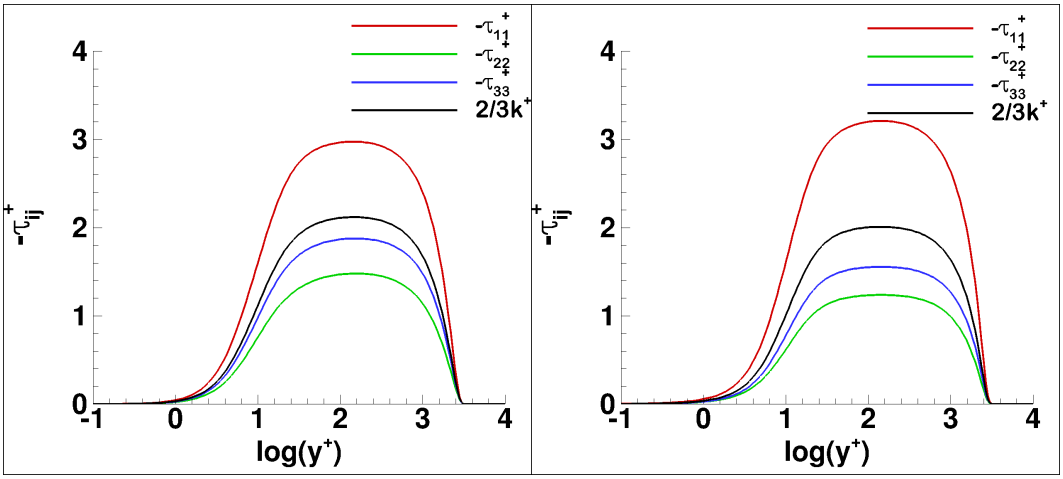


(a) k-kL-ARSM ARSM based on SSG.

(b) SSG RSM-kL.

Figure 5. Flat plate case, kL ARSM and RSM results.

k-kL-QCR and LRR RSM-kL. It is interesting that both models give similar normal stress behavior, for example the spanwise normal stress ($\tau_{33}$) is very close to half of the other two components:

$$\tau_{22}^{+} \approx \frac{1}{2}\left(\tau_{11}^{+} + \tau_{33}^{+}\right) \tag{32}$$

This behavior is completely different from the results generated by DNS [37] and LES [38] for subsonic flat plate flow. This behavior may not have any influence on the results produced by either kL turbulence models for attached or separated flow. It is quite possible that such behavior will affect any flow that is driven by the increment between normal stress components such as flow through a square duct discussed in subsection 4.8.

## 4.2 Subsonic/Transonic Cold Jet Cases

In the experiment, the axisymmetric jet exits into quiescent (nonmoving) air at two nozzle exit Mach conditions, $M_{exit,acoustic} = u_{jet}/a_{\infty} = 0.51$ and 0.9, respectively (see Table 3). However, because simulating flow into totally quiescent air is difficult to achieve for some

Table 3. Subsonic/Transonic cold jet conditions.

| Set Point | $Mach_{exit,acoustic}$ | NPR | NTR | $T_{jet,static}/\ T_{\infty}$ |
|---|---|---|---|---|
| 3 | 0.51 | 1.197 | 1.0 | 0.950 |
| 7 | 0.90 | 1.861 | 1.0 | 0.835 |

CFD codes, the solution is computed with a very low background ambient condition of $M_{\infty}$ = 0.01, moving left-to-right in the same direction as the jet. Figure 7 shows the grid and flow setup for the subsonic jet case. First, we evaluate grid convergence for the jet correction

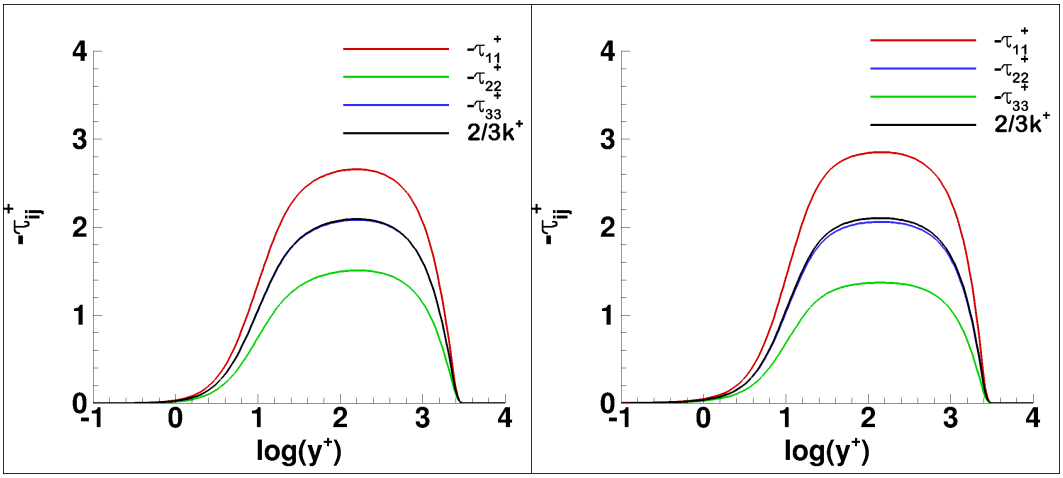


(a) k-kL-QCR. (b) LRR RSM-kL.

Figure 6. Flat plate Reynolds Stress results using k-kL-QCR and LRR RSM-kL.

using three grid levels taken from reference 10. The grids have 9,271, 36,621, and 145,561 nodes (coarse, medium, and fine).

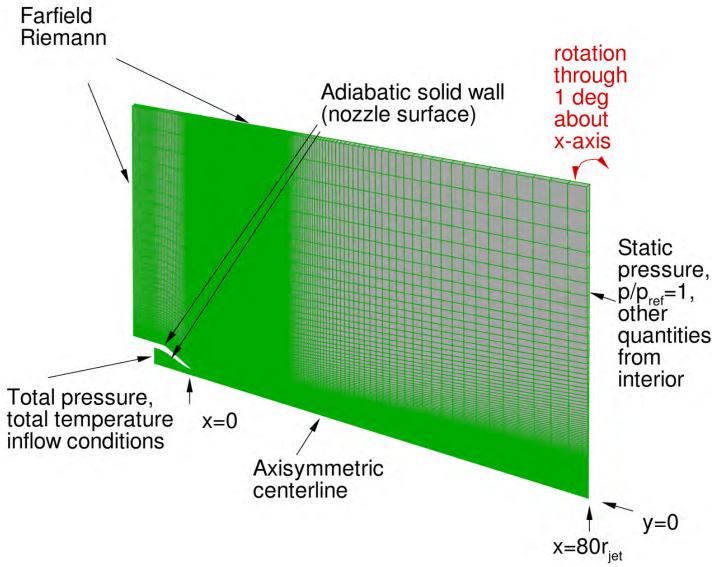


Figure 7. ARN1 nozzle and boundary conditions.

This jet correction model, including both free shear and compressibility correction terms, is termed k-kL+J. Figure 8 shows the centerline velocity results using the three grid levels. The medium and fine grid levels yield nearly identical results, indicating sufficient grid convergence of the jet correction option. With the medium grid, compared the ability of the k-kL+J turbulence model to predict this jet flow with the basic k-kL and SST turbulence models (see figs. 9 and 10).

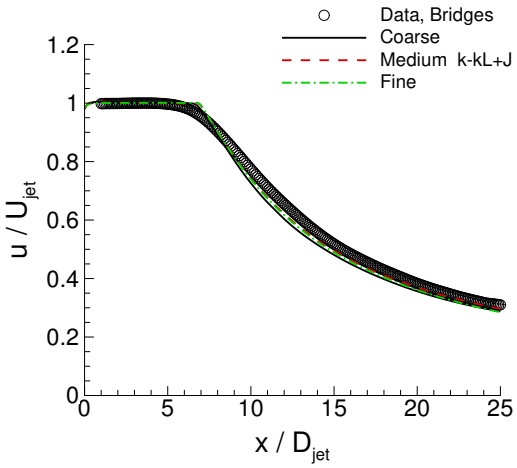


Figure 8. Grid sensitivity, streamwise centerline velocity, Set Point 3. Symbols, Data-Bridges [19].

The jet core length and rate of decay are better predicted when using the k-kL+J model, as shown in figure 9(a) for Set Point 3. In particular, the jet core length is in better agreement with the experiment than the much longer core predicted using the SST turbulence model. Similarly, in figure 9(a) for Set Point 7, the k-kL+J model produces the best results as compared with experimental data and other turbulence models. Very good comparisons of the k-kL+J are shown in figure 10(a) for set point 3 and in figure 10(b) for set point 7 for the velocity variations with radial direction at different $x/D_{jet}$ locations.

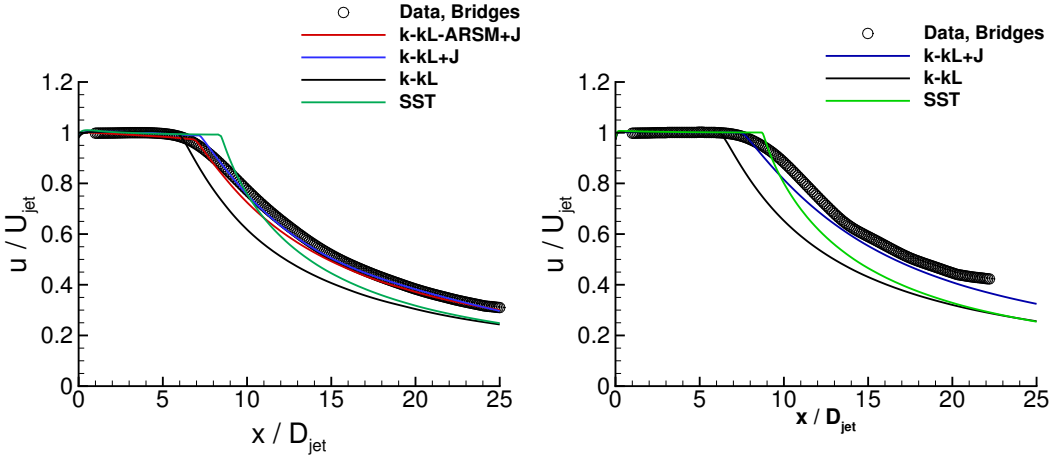


(a) Set Point 3 flow condition.

(b) Set Point 7 flow condition.

Figure 9. Streamwise centerline velocity profiles using different linear RANS turbulence models. Symbols, Data-Bridges [19]; lines, FUN3D.

The jet core length and rate of decay are very similar when using either k-kL-ARSM or k-kL+J turbulence models as shown in figure 11(a). Slight differences are observed between these models in predicting turbulent kinetic energy as shown in figure 11(b). This verifies that the ARSM is almost inactive away from walls. This results from using the blending

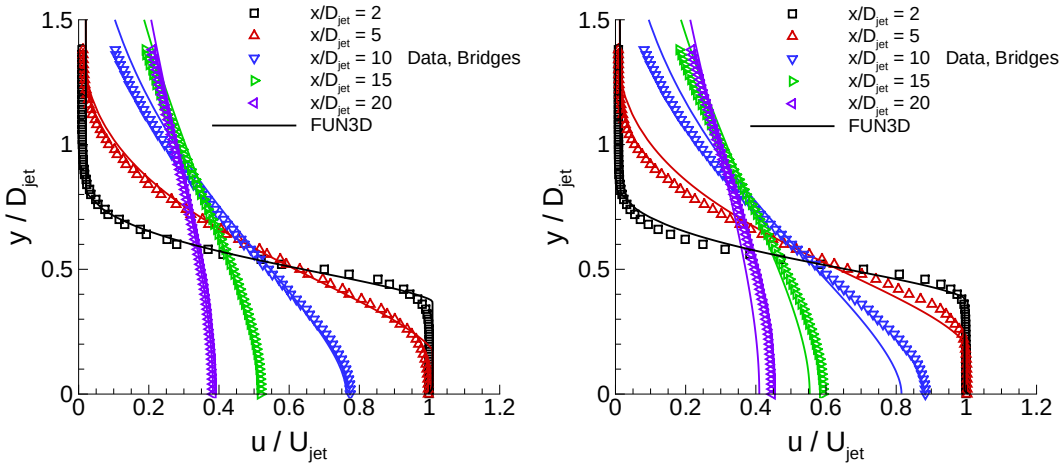


(a) Set Point 3 flow condition.

(b) Set Point 7 flow condition.

Figure 10. Velocity variations with radial direction at different $x/D_{jet}$ locations using k-kL+J turbulence model. Symbols, Data-Bridges [19]; lines, FUN3D.

function $f_2$ (eqs. 27 and 25) to switch between linear and nonlinear production.

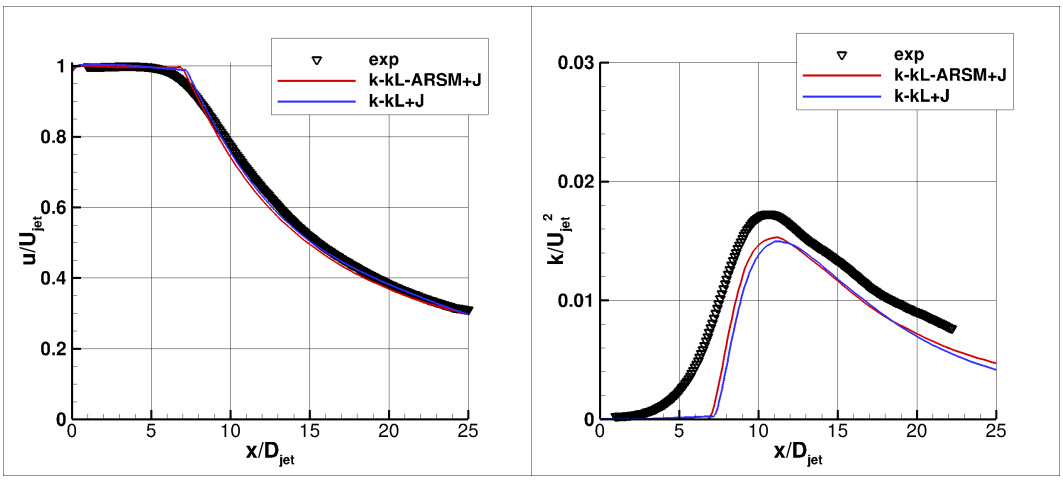


(a) Streamwise centerline velocity.

(b) Streamwise centerline turbulence kinetic energy.

Figure 11. Comparison between linear and nonlinear k-kL turbulence model Symbols, Set Point 3 Data-Bridges [19]; lines, FUN3D.

## 4.3 Subsonic Hot Jet Cases

In this section, we evaluate the results of the "+T" correction for Set Points 23, 29, and 46, as listed in Table 4. These cases cover a range of jet total conditions with pressure

Table 4. Subsonic hot jet conditions.

| Set Point | $Mach_{exit,acoustic}$ | NPR | NTR | $T_{jet,static}$ / $T_\infty$ |
|---|---|---|---|---|
| 23 | 0.50 | 1.102 | 1.81 | 1.762 |
| 29 | 1.33 | 1.888 | 2.11 | 1.762 |
| 46 | 0.90 | 1.219 | 2.86 | 2.700 |

ratios, $1.1 < \text{NPR} < 1.888$ and temperature ratios, $1.81 < \text{NTR} < 2.86$. Set Point 46 has the highest jet total temperature tested. As a result, the exit Mach number is elevated compared to a cold jet of the same total pressure ratio. Figure 12(a) shows the centerline velocity results using three grid levels. The medium and fine grid results are very close indicating reasonable grid convergence when using the temperature correction option. Figure 12(b) shows the temperature correction function variation for Set Point 46. As expected, the correction is highly active in the region with high-temperature gradients, as shown by the regions colored red. In effect, the turbulence viscosity is higher, causing faster mixing than what would be predicted using the basic turbulence model with no correction. In the regions with no temperature gradient, i.e., inside the nozzle and in the farfield, the correction reverts to a value of 1, as shown by the regions colored blue.

In addition, two more Set Points were selected to validate the temperature correction model. Set Point 23 with NTR of 1.81 and with a lower subsonic jet flow, and Set Point 29 with higher NTR of 2.11 with a higher supersonic jet flow. Both cases behave similarly to Set Point 46 and have similar grid convergence (not shown). These cases are shown in figures 13(a) and (b) using the fine grid level. The "+J+T" option produces better results than the "+J" correction alone for the centerline axial velocity as compared with experimental data.

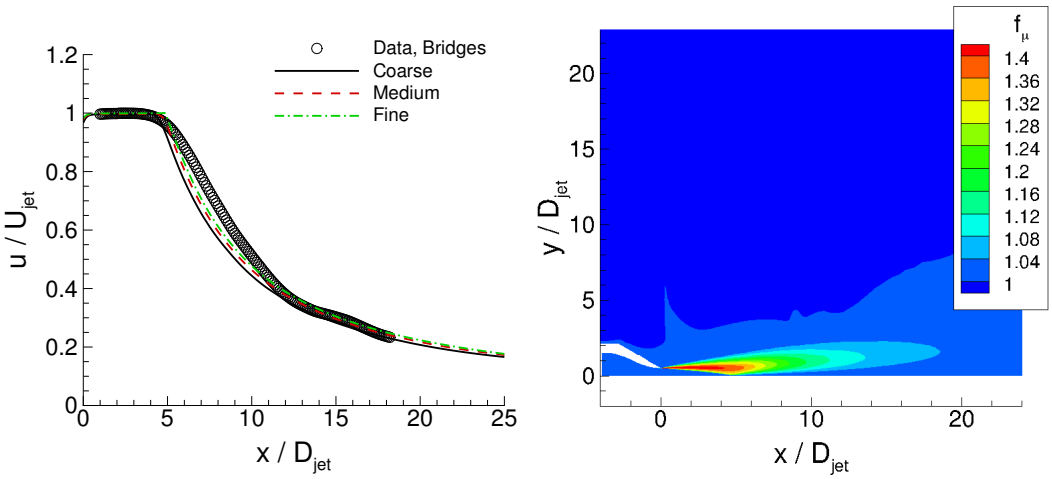


(a) Grid sensitivity, streamwise centerline velocity. Symbols, Data-Bridges [19]; lines, k-kL+J+T.

(b) Temperature correction function contours.

Figure 12. ARN1 hot subsonic jet, Set Point 46.

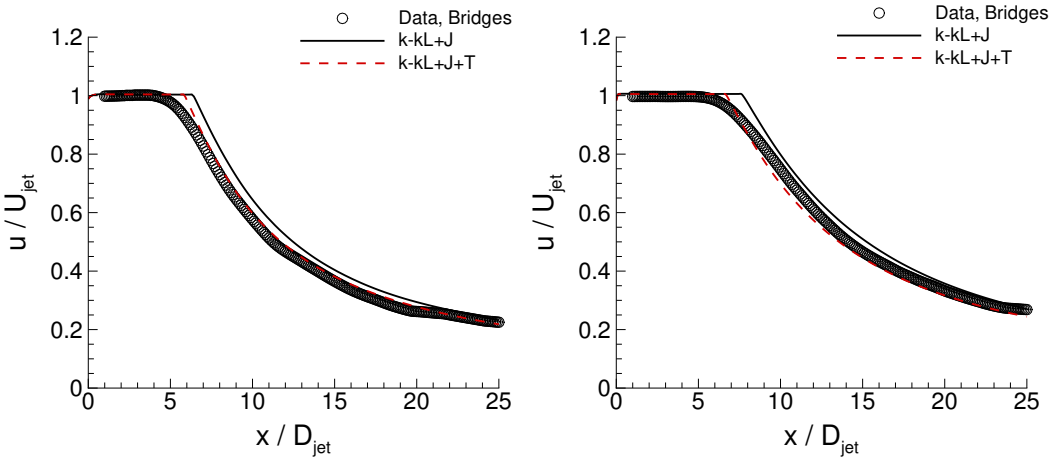


(a) Set Point 23.

(b) Set Point 29.

Figure 13. Streamwise centerline velocity, ARN1 hot subsonic jets. Symbols, Data-Bridges [19], lines, fine grid.

## 4.4 High-Speed Mixing Layer

In this case, subsonic and supersonic streams, initially separated by a splitter plate, come into contact and form a shear layer. Results are compared with test case 4 in the experiment of Goebel and Dutton [20]. At the entrance of the mixing layer, the flow conditions are $M_1$ = 2.34, $T_{t1}$ = 360 K, and $U_1$ = 616 m/s for the high-speed stream and $M_2$ = 0.3, $T_{t2}$ = 360 K, and $U_2$ = 100 m/s for the low-speed stream. For this case, the convective Mach number, $M_c$, is 0.86. For $M_c > 0.5$, the flow is considered compressible, and compressibility correction through the use of +J correction is expected to improve the prediction. Figure 14 shows the flow setup for the high-speed mixing layer case. Figure 15 shows the effect of using +J correction in the prediction of the high-speed mixing layer at x = 100 mm. The raw data of the velocity correctly matches the experimental data using +J correction as shown in figure 15(a). The shear stress profile and peak value are in very good agreement using +J correction with experimental data as shown in figure 15(b).

We have used k-kL+J, k-kL-ARSM+J, SST, and LES [39] turbulence models and compared the results with the experimental data as shown in figures 16, 17, and 18. Figure 16(a) shows the raw data comparisons between the three turbulence models and experimental data for raw velocity profile at x = 100 mm downstream of the splitter plate. Both k-kL turbulence models show good results when compared with the other models. The LES results were offset from the other turbulence model results and experimental data. As the mixing layer flow developed, a self similar flow profile could be used to report the results. Using this approach, we plotted the velocity normalized values, $u^n$ versus the normalized distance $y^n$ instead of the raw data:

$$y^n = \frac{y - y_{0.5}}{b} \; and \; u^n = \frac{U - U_2}{\Delta U} \; , \tag{33}$$

$$b = y_{0.9} - y_{0.1} \; and \; \Delta U = U_1 - U_2 \tag{34}$$

$$y_r \; at \; u^n = r \tag{35}$$

Figure 16(b) shows the comparisons between the three turbulence models, normalized results and experimental data. The results are similar using this approach. However, the SST results were still missing the data at the edge of the mixing layer. Figure 17(a) shows the

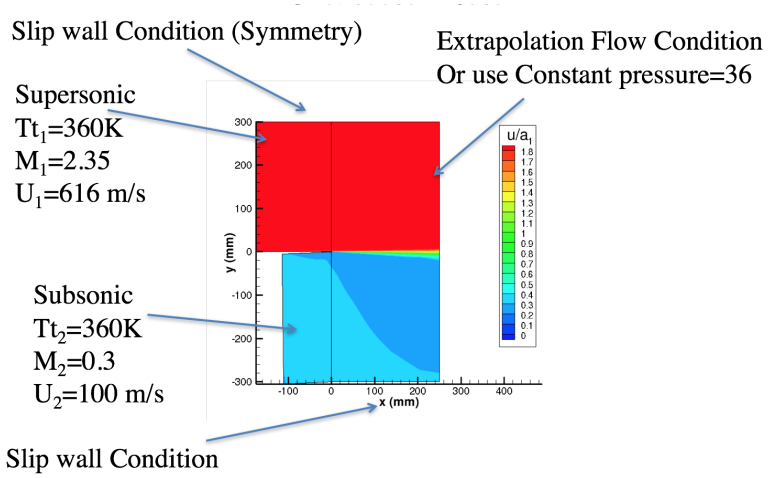


Figure 14. Mixing layer case 4, $M_c = 0.86$.

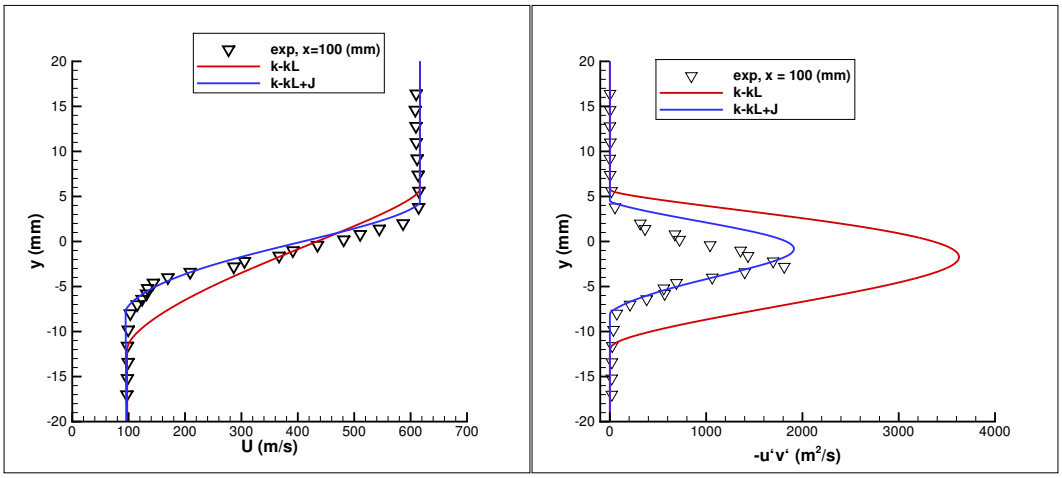


(a) Raw velocity results.

(b) Raw shear stress results.

Figure 15. 2D Mixing Layer: Effect of +J correction in the prediction of high-speed mixing layer at x = 100mm.

data comparisons between the three turbulence models and experimental data for raw shear stress at x = 100 mm downstream of the splitter plate. Both k-kL turbulence models show good results when compared with the data from the other models. The shear stress results from the k-kL and LES turbulence models are comparable with the experimental data. The LES results were again offset from the other turbulence model results and experimental data. Now, we normalize the shear stress by the square of the velocity difference as

$$\frac{-u'v'}{\Delta U^2}$$

Figure 17(b) shows the normalized results. It is clear that the LES and k-kL produced better results compared with experimental data than results from the SST turbulence model.

Figure 18 shows the change of shear layer thickness, b, with distance, x, from the end of the splitter plate comparisons with experimental data. The medium and fine grid results

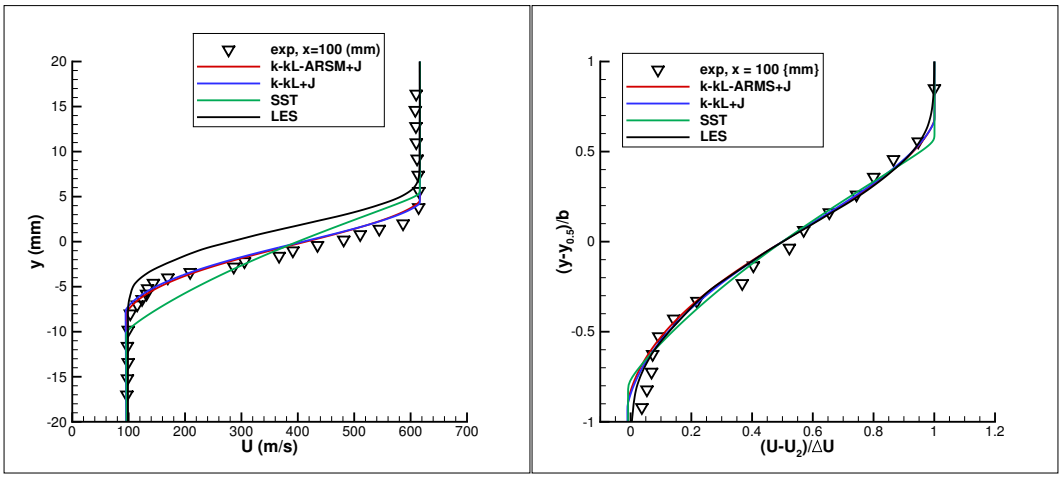


(a) Raw results. (b) Normalized results.

Figure 16. 2D Mixing Layer: Comparison of turbulence models velocity results at x = 100 mm.

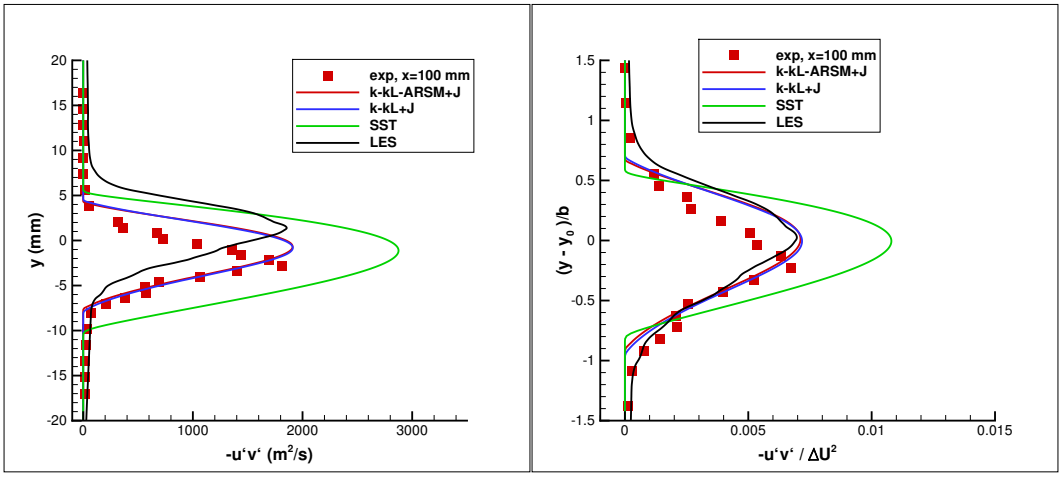


(a) Raw results. (b) Normalized results.

Figure 17. 2D Mixing Layer: Comparison of turbulence model shear stress results at x = 100 mm.

are very similar indicating grid convergence as shown in figure 18(a). The k-kL turbulence models are comparable with the LES results and closer to the experimental data when compared with SST results as shown in figure 18(b).

In general, all of the turbulence models examined appear to predict the streamwise velocity profiles, it appears that the k-kL is much better than the two-equation SST model. Overall, they are closer to the experimental values in predicting the turbulence intensity, turbulent shear stress, and shear layer thickness. The results using the k-kL are in very good agreement with experimental and LES data.

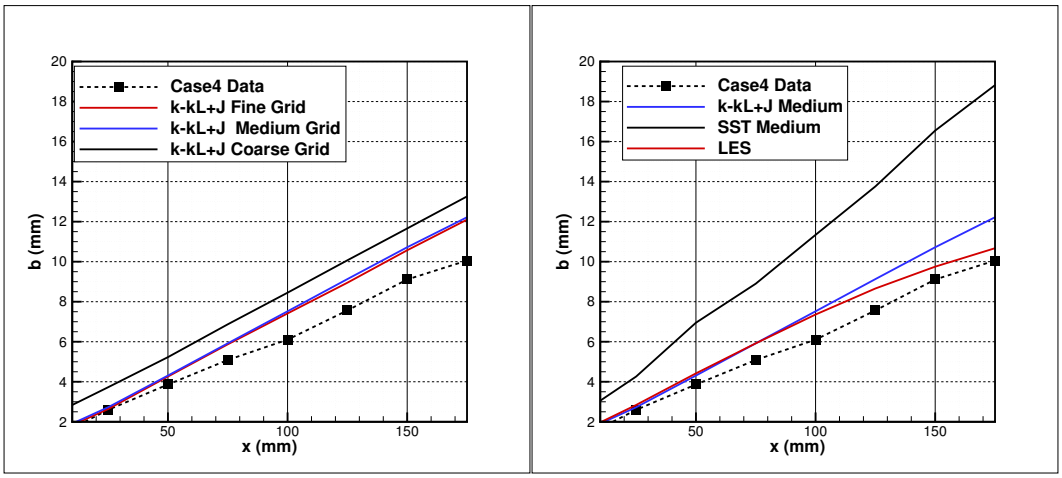


(a) Grid sensitivity.

(b) Turbulence models comparisons.

Figure 18. Shear layer thickness comparisons for different turbulence models.

## 4.5 2D NASA Subsonic Wall-Mounted Hump

Figure 19 shows a sketch of the 2D NASA wall-mounted hump test case with boundary conditions used in this analysis. The model is mounted between two glass endplate frames, and both leading and trailing edges are faired smoothly with a wind tunnel splitter plate [21]. This is a nominally two-dimensional experiment, treated as such for the CFD validation. The primary focus of this case is to assess the ability of turbulence models to predict 2D separation from a smooth body (caused by adverse pressure gradient) as well as subsequent reattachment and boundary layer recovery. Since its introduction, this particular case has proved to be a challenge for all known RANS models. Models tend to underpredict the turbulent shear stress in the separated shear layer, and therefore, tend to predict too long a separation bubble. For this case, the reference freestream velocity is approximately 34.6 m/s (M = 0.1). The back pressure is chosen to achieve the desired flow. The upstream "run" length is chosen to allow the fully turbulent boundary layer to develop naturally, and achieve approximately the correct boundary layer thickness upstream of the hump. The upper boundary is modeled in the CFD as an inviscid (slip) wall, and it includes a contour to its shape to approximately account for the blockage caused by the end plates in the experiment. The grid size is 91,718 nodes with hex cells. Menter et al. [3–5] noticed that the kL-based turbulence models produce under- and over-shoot of the skin friction in the separated flow region as shown in figure 20(a) using $C_{13} = 1.0$ from equation 10. This is the only quantity that shows such behaviour. To reduce these jumps in skin friction, a $C_{13}$ value of 0.5 is selected for the linear k-kL two-equation turbulence model. For ARSM and RSM, we used a value of 0.25. $C_{13}$ has very minimal effect in other quantities as shown for shear stress at x/c = 1.1 (see figure 20(b).

This case is used to calibrate ARSM to optimize the results. The basic ARSM completely missed the separation and reattachment locations as shown in figure 21(a). Adjusting $a_2$ to 0.8 from 0.7 and limiting the $kL$ production ($P_{kL}$) as shown in equation 17 significantly improves the results of ARSM. Limiting $P_{kL}$ allows the RANS model to overcome the deficit in predicting shear stress level as shown in figure 21(b). This combination produces the best results for skin friction and other flow quantities such as velocity and shear stress. For the RSM, we only limit the $P_{kL}$ with no need to change any other parameters. The effect of this limiting was first observed using RSM and was successfully applied to ARSM.

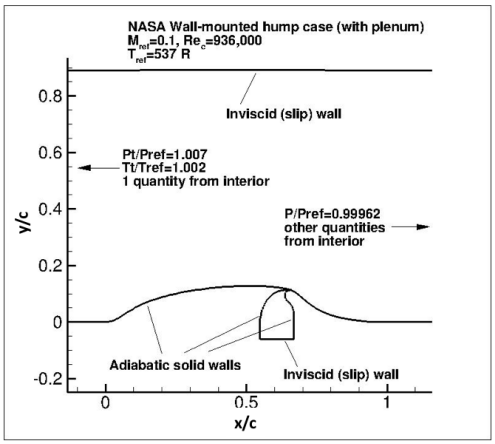


Figure 19. Wall-Mounted Hump and boundary conditions.

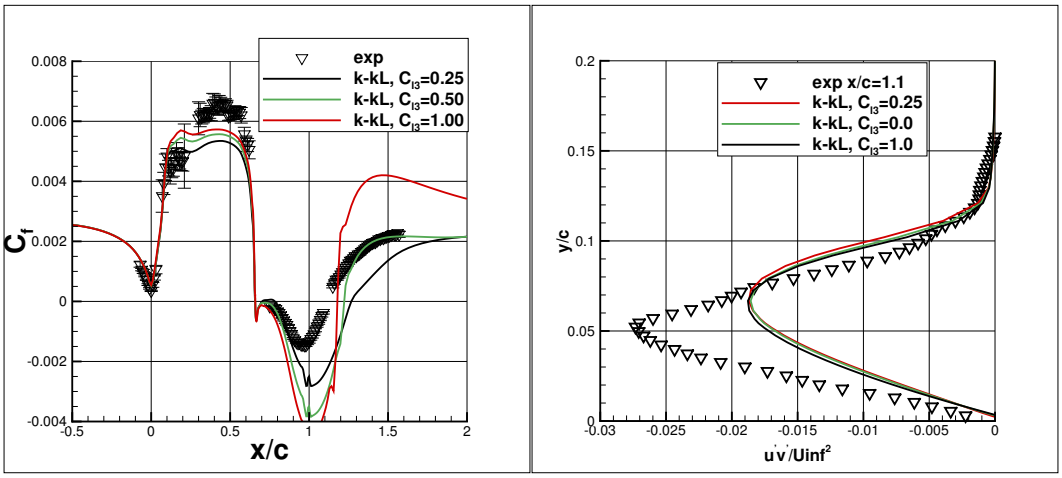


(a) Skin friction results.

(b) Shear stress results.

Figure 20. Wall-Mounted Hump: calibration of k-kL turbulence model.

Figure 22 shows the comparisons between two-equation turbulence models and experimental data. The ARSM gives the best skin friction results as compared with other models and experimental data. All kL formulations missed the peak in $C_f$ near x/c = 0.4. SST is the only model that predicted skin friction peak. However, SST completely missed shear stress peak and yielded, separation bubble size similar to k-kL-QCR and k-kL. All kL formulations improve the prediction of the shear stress peak with the best results generated using the k-kL-ARSM. Figure 23 shows velocity streamline coloured by u-velocity. Table 5 reports separation and reattachment locations, bubble size and % error results from different turbulence models. The experimental data bubble size was 0.435c. The k-kL, SST and k-kL-QCR have larger bubble size than experimental data (figures 23(b), (c) and (d)) with 33.7, 41.6, and 43.2% error, respectively. Out of all two-equation turbulence models, k-kL-ARSM produces bubble size that is close to the experimental data with 3.4% error (figure 23(a)). The full Reynolds stress RSM-kL had an error of 6.0%. All turbulence models closely predicted the location of separation around x/c = 0.66. However, only k-kL-ARSM

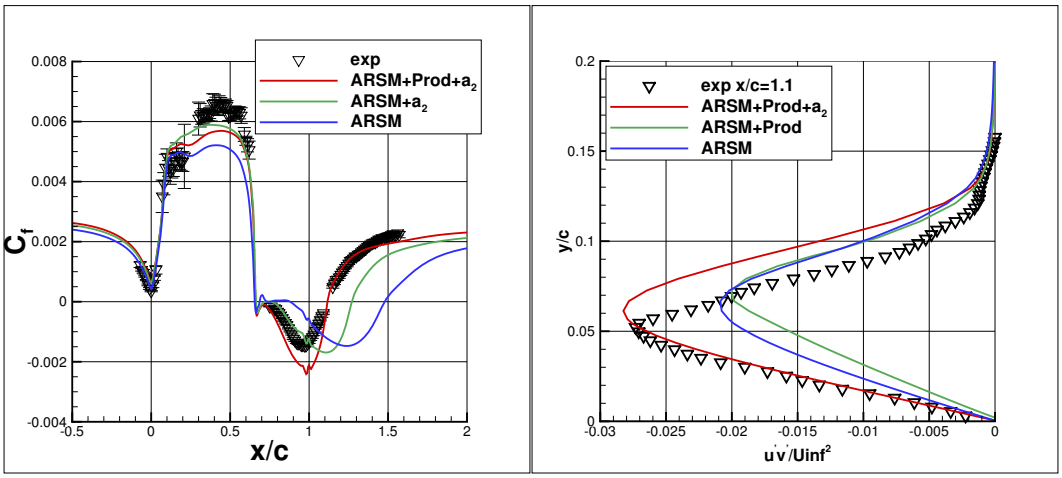


(a) Skin friction results. (b) Shear stress results.

Figure 21. Wall-Mounted Hump: Calibration of k-kL+ARSM turbulence model.

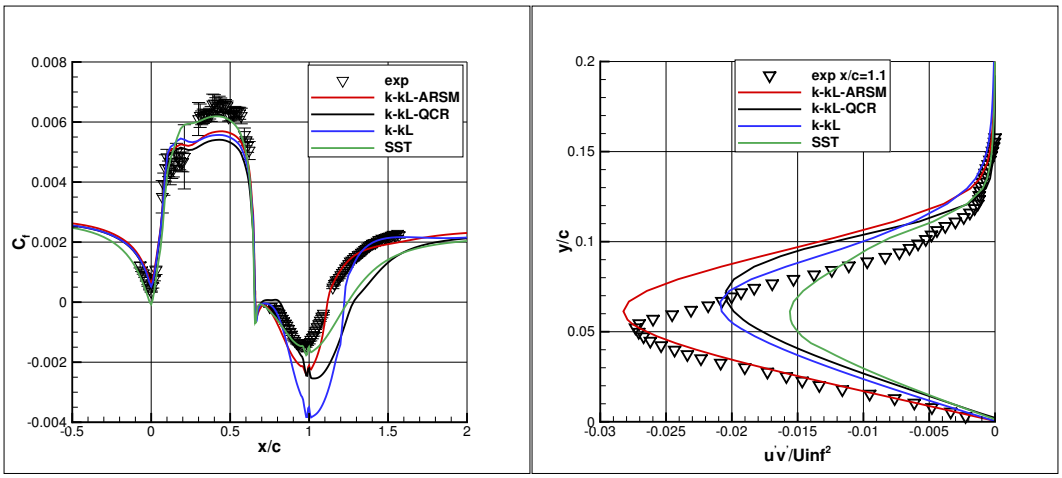


(a) Skin friction results. (b) Shear stress results.

Figure 22. Wall-Mounted Hump: Skin friction and shear stress using two-equation turbulence models.

and RSM-kL closely predict the reattachment location around x/c = 1.1. As a result, these models have the smallest % error. However, ARSM uses less than half the computer resources needed by RSM. This makes ARSM a more attractive model to use because it has similar modeling capabilities to RSM.

Figure 24 shows comparisons of two-equation turbulence models (k-kL-ARSM, k-kL, and SST) velocity at different x/c locations in the separation bubble. At x/c = 0.8 and 0.9, all models have similar velocities in this location close to the separation location (x/c = 0.66). The flow is observed to reattach near x/c = 1.1 in the experiment. The linear turbulence models (SST and k-kL) are still separated and the nonlinear (k-kL+ARSM) is reattached. This is clearly shown in figures 24(c) and (d) at x/c=1.1 and 1.3, respectively. At x/c = 1.3, SST and k-kL are showing reverse flow close to the wall. The result from

Table 5. Wall-Mounted Hump: Separation and reattachment locations.

| Results | Separation x/c location | Reattachment x/c location | Bubble Size (c) | % Error |
|---|---|---|---|---|
| Experimental data | 0.665 | 1.100 | 0.435 | — |
| SST | 0.654 | 1.270 | 0.616 | 41.6 |
| k-kL | 0.658 | 1.240 | 0.582 | 33.7 |
| k-kL-QCR | 0.657 | 1.280 | 0.623 | 43.2 |
| k-kL-ARSM | 0.660 | 1.110 | 0.450 | 3.4 |
| RSM-kL | 0.660 | 1.069 | 0.409 | 6.0 |

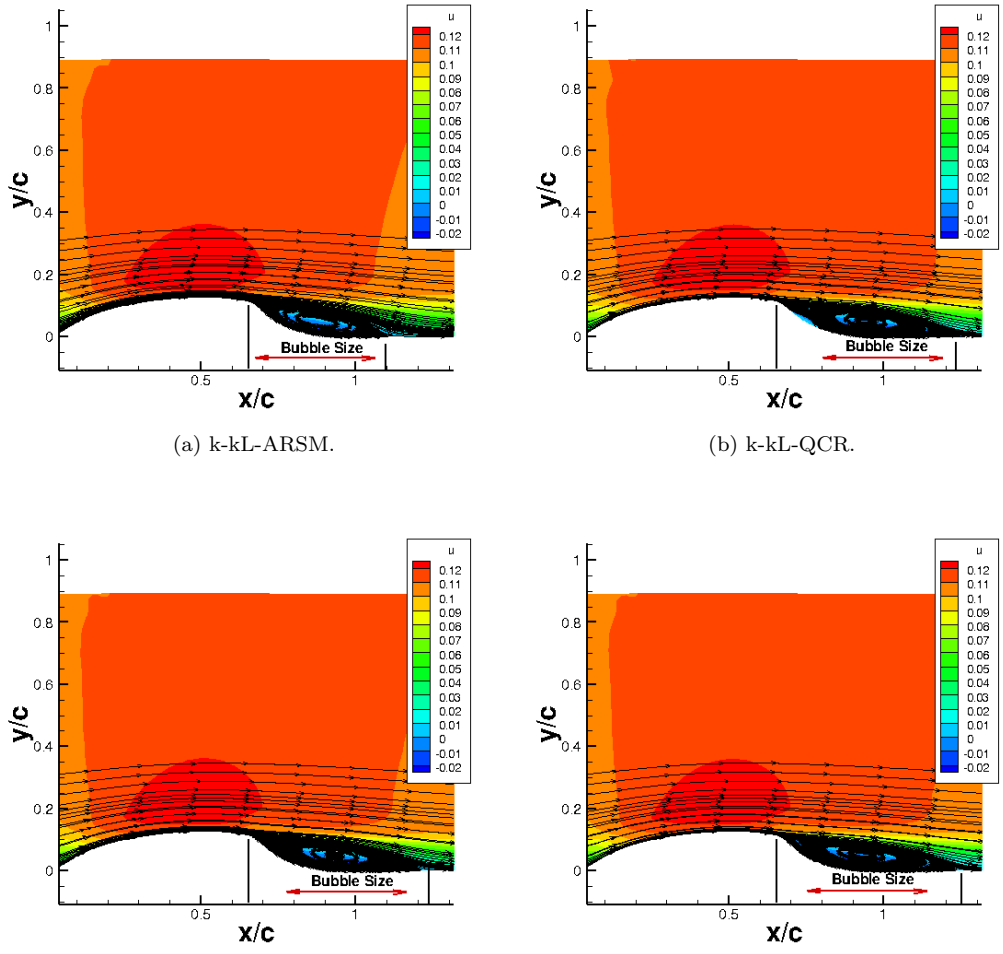


(a) k-kL-ARSM.

(b) k-kL-QCR.

(c) k-kL.

(d) SST.

Figure 23. Wall-Mounted Hump: Separation bubble size comparisons using different two-equation turbulence models.

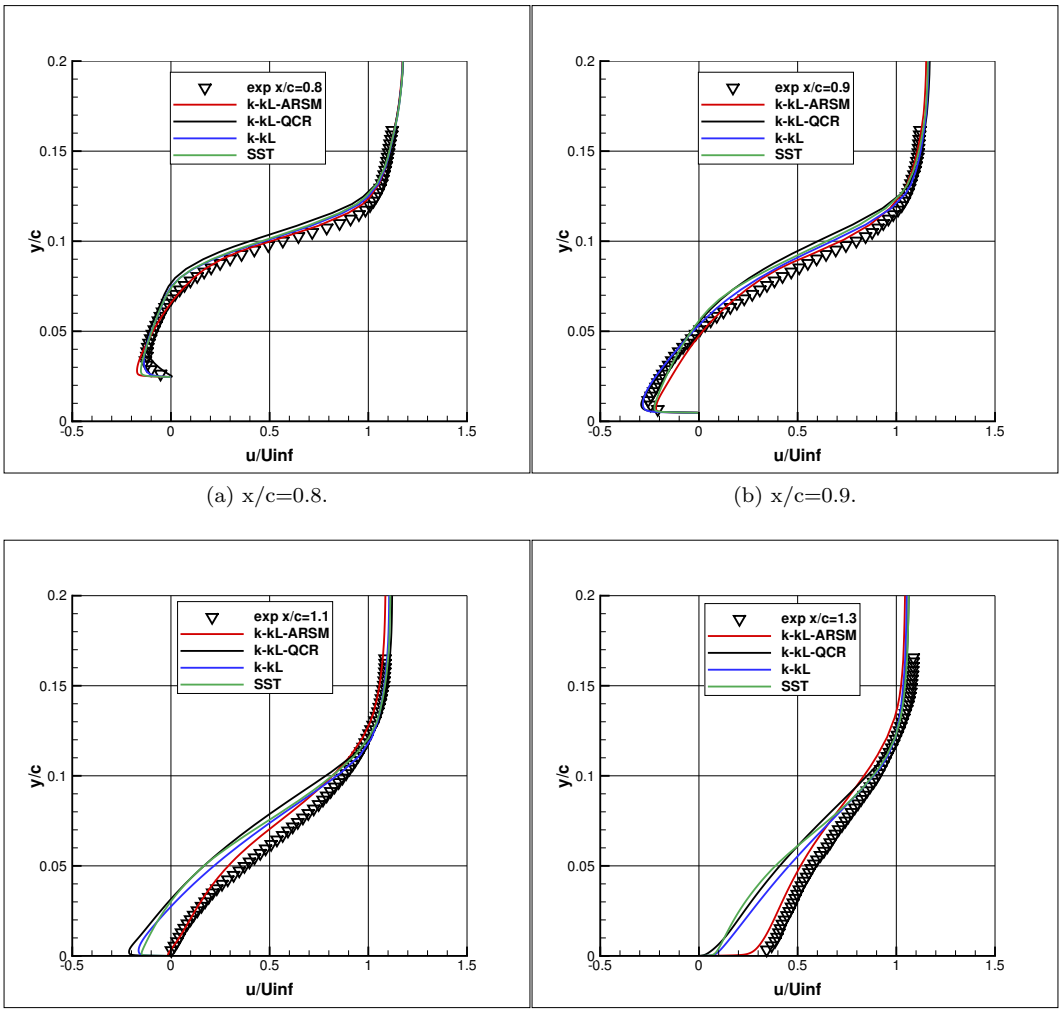


(a) x/c=0.8. (b) x/c=0.9.

(c) x/c=1.1. (d) x/c=1.3.

Figure 24. Wall-Mounted Hump: Comparison of two-equation turbulence model velocity results.

k-kL-ARSM is attached at this location. Figure 25 shows a comparison of the two-equation turbulence model shear stress results. In general, RANS turbulence models underpredict the level of shear stress by up to 50% for this hump case. This is clearly illustrated in figure 25 from the results of the SST and k-kL models. However, the present k-kL-ARSM shows the capability of producing similar levels of shear stress to the experimental data at x/c of 0.8 to 1.3. Figure 26 shows comparisons of RSM turbulence models velocity results at different x/c locations. We are showing results from LRR, SSG, and LRR+C. All RSMs produce good comparisons with experimental data. However, RSM results require at least twice the computation time of two-equation turbulence models. Also, these models are very stiff and require smaller time steps. Figure 27 shows comparisons of RSM turbulence models shear stress results at different x/c locations. In general, RSM results are comparable with shear stress levels from experimental data. From the results presented in this section, it is clear that k-kL-ARSM produces the best results from all the kL formulations with the least computational resources.

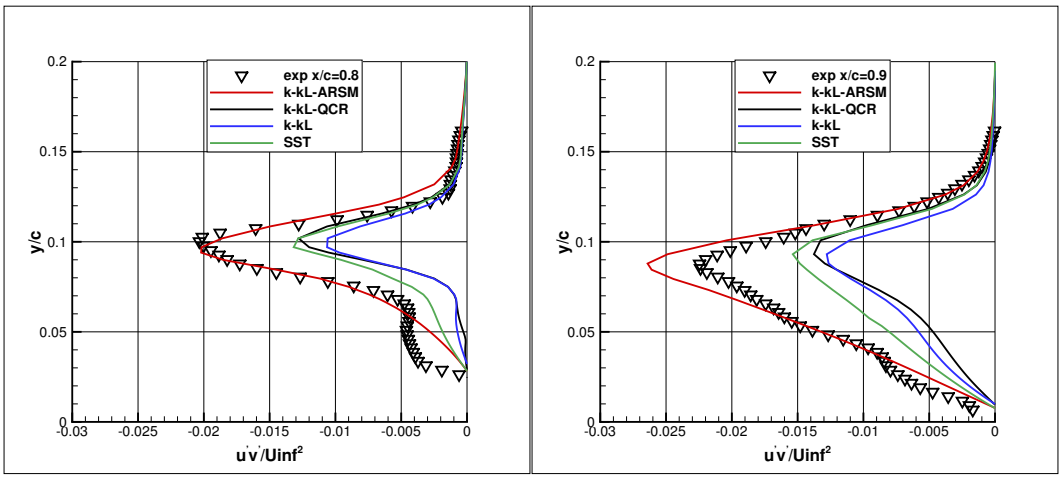


(a) x/c=0.8.




(b) x/c=0.9.

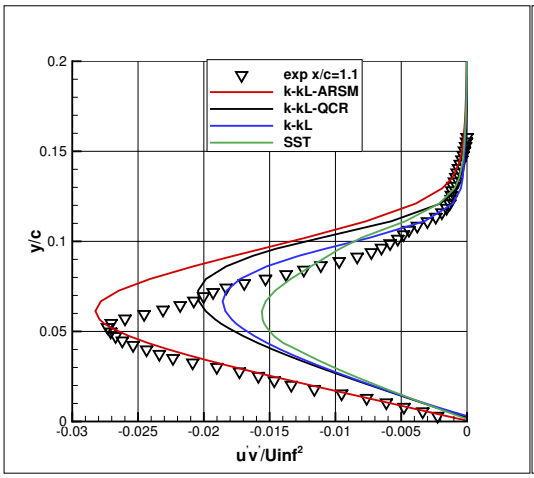


(c) x/c=1.1.

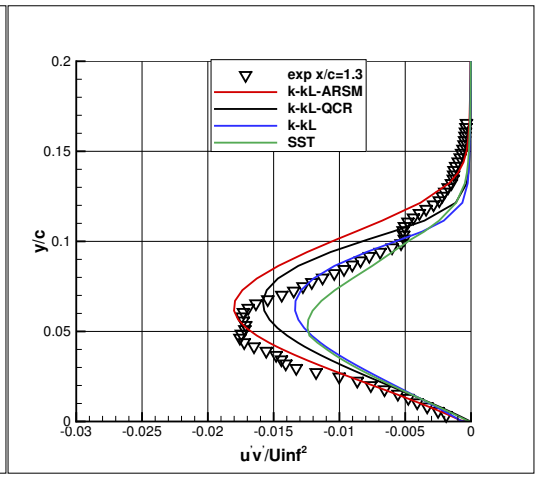


(d) x/c=1.3.

Figure 25. Wall-Mounted Hump: Comparison of two-equation turbulence model shear stress results.

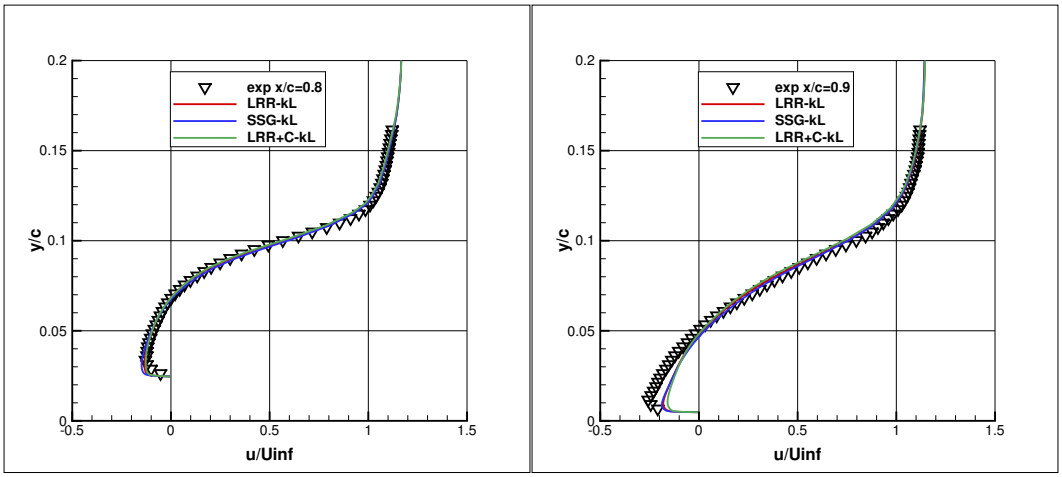


(a) x/c=0.8.




(b) x/c=0.9.

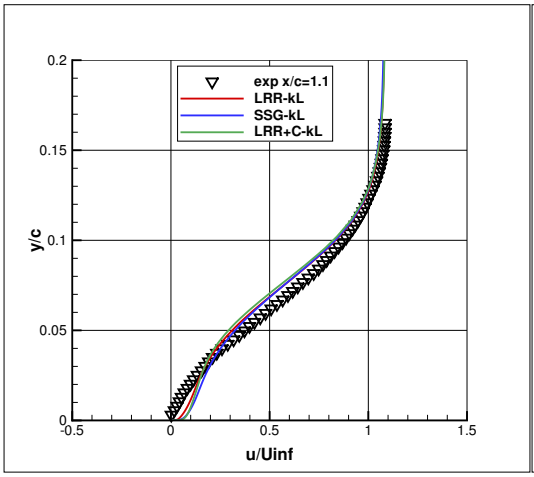


(c) x/c=1.1.

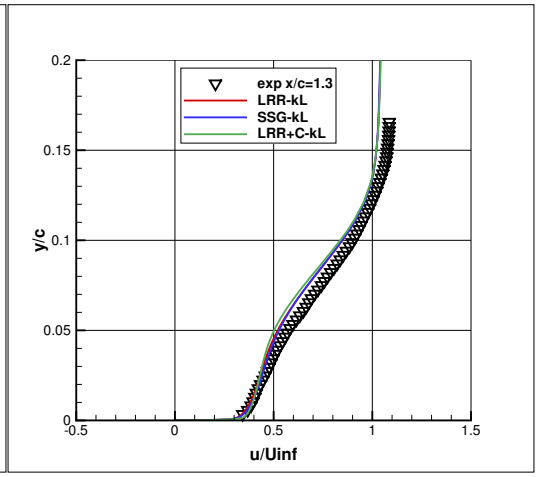


(d) x/c=1.3.

Figure 26. Wall-Mounted Hump: Comparison of RSM turbulence model velocity results.

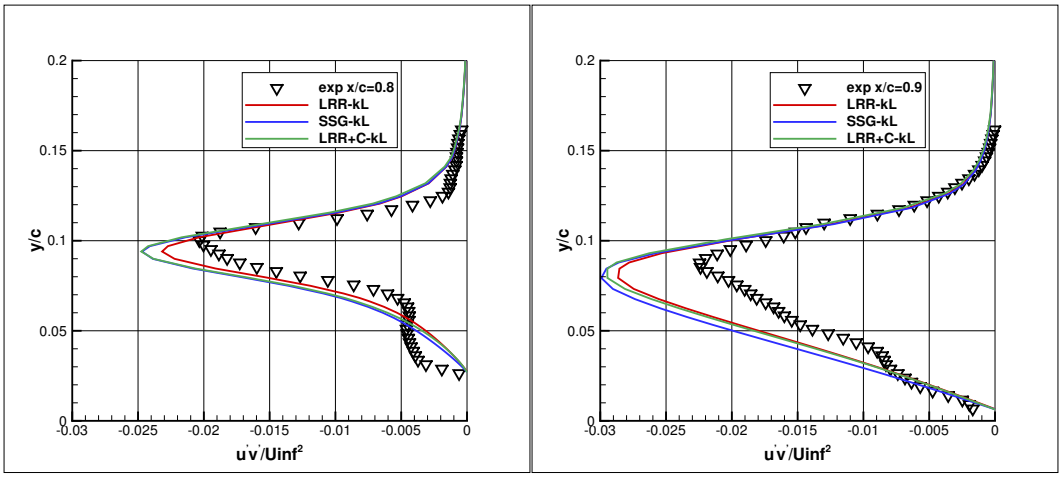


(a) x/c=0.8.




(b) x/c=0.9.

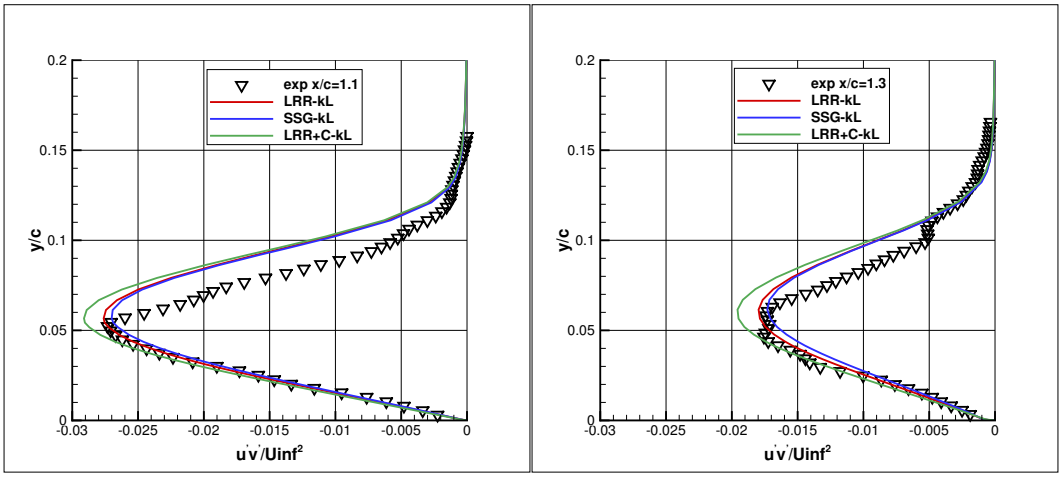


(c) x/c=1.1.




(d) x/c=1.3.

Figure 27. Wall-Mounted Hump: Comparison of RSM turbulence model shear stress results.

The corrections introduced in sections 3.4.1 and 3.4.2 should not have any effect on the results for this test case with no high-temperature or high-speed shear flow. Figure 28 shows that there is no significant difference in the results using turbulence model corrections for either k-kL or k-kL-ARSM.

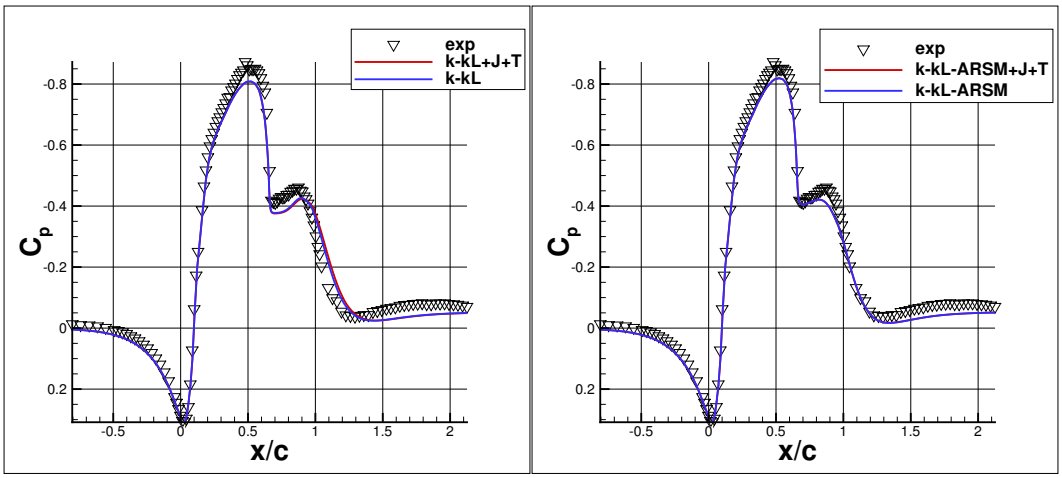


(a) k-kL. (b) k-kL-ARSM.

Figure 28. Wall-Mounted Hump: Effect of jet and temperature corrections.

## 4.6 Transonic Bump

This shock-induced separation case at transonic speed adds complexity to modeling separated flow. Also, axisymmetry removes the difficulty experienced when conducting the experiment than for the two-dimensional flow experiment. Figure 29 shows a sketch of the axisymmetric transonic bump case with boundary conditions used in this analysis. This is a transonic, $M_\infty = 0.875$ case at Re = 2.763 million based on L = chord length. The purpose here is to provide a validation case that establishes the models ability to predict separated flow. For this particular axisymmetric transonic bump case, the experimental data are from Bachalo and Johnson [22]. The experiment utilized a cylinder of 0.152 m diameter in a closed return, variable density, and continuous running tunnel with 21% open porous-slotted upper and lower walls. The boundary layer incident on the bump was approximately 1 cm thick. The bump chord was 0.2032 m. In the experimental case, with a freestream Mach number of 0.875, the shock and trailing-edge adverse pressure gradient results in flow separation with subsequent reattachment downstream.

The majority of RANS turbulence models fails to predict the correct reattachment of this separated flow case, with the separation bubble size overpredicted by up to 23.7% as reported in Table 6 using SST. The k-kL cuts the error by more than 50%. The k-kL-QCR slightly improves the results to 18.75%, whereas the k-kL-ARSM stayed closer to the k-kL at 13%. The most improvement results from using the RSM-kL at 7.1%. Figure 30(a) shows surface pressure comparisons between two-equation kL and SST turbulence models with experimental data [22]. SST predicts a further upstream location of the shock at x/c = 0.65 compared with experimental data at 0.66, but it produces the best profile in the x/c region of 0.8 through 1.2. Figure 30(b) shows typical velocity contours from most two-equation turbulence models. Next, we evaluate the capabilities of these models in predicting shear stress magnitudes. Figure 31 shows that k-kL-ARSM improves the result at x/c = 0.813. However, there are no improvements from any of the models at x/c = 1.375. For the velocity

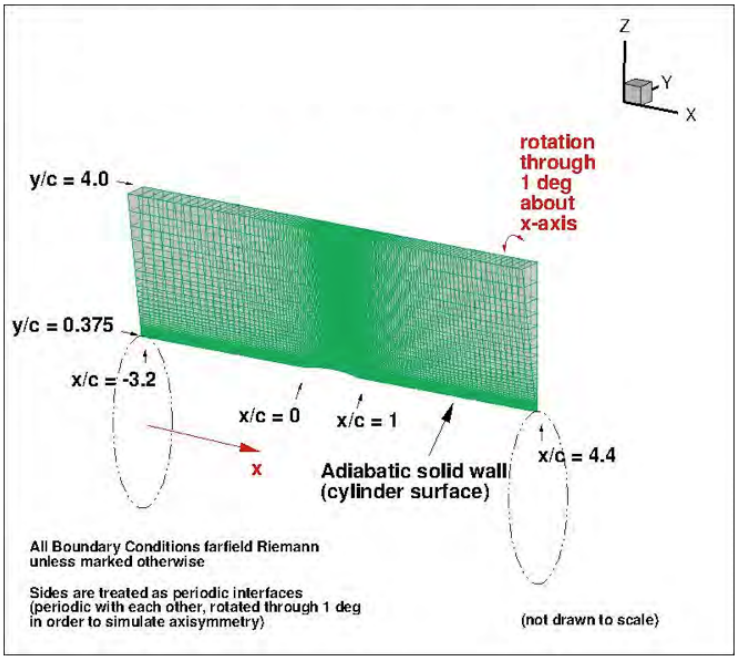


Figure 29. Transonic Bump and boundary conditions.

Table 6. Transonic Bump: Separation and reattachment locations.

| Results | Separation x/c location | Reattachment x/c location | Bubble Size (c) | % Error |
|---|---|---|---|---|
| Experimental data | 0.700 | 1.100 | 0.400 | — |
| SST | 0.665 | 1.160 | 0.495 | 23.7 |
| k-kL | 0.669 | 1.120 | 0.451 | 12.7 |
| k-kL-QCR | 0.665 | 1.140 | 0.475 | 18.75 |
| k-kL-ARSM | 0.701 | 1.050 | 0.349 | 13.0 |
| RSM-kL | 0.660 | 1.069 | 0.409 | 7.1 |

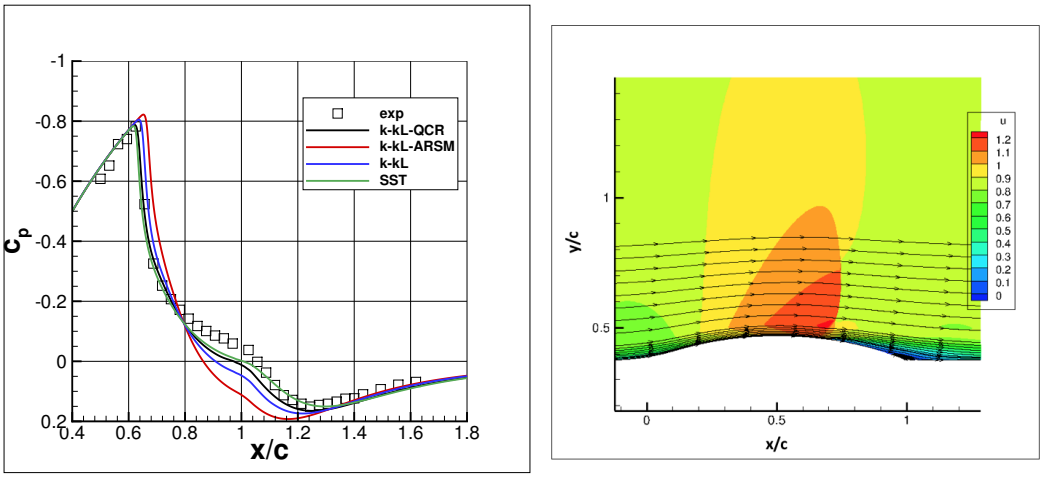


(a) Surface pressure.

(b) Typical velocity contours.

Figure 30. Axisymmetric Transonic Bump : Comparison of two-equation turbulence model results.

results, k-kL-ARSM improves the results at x/c = 1.375 and notable improvements at x/c = 0.813 as shown in figure 32.

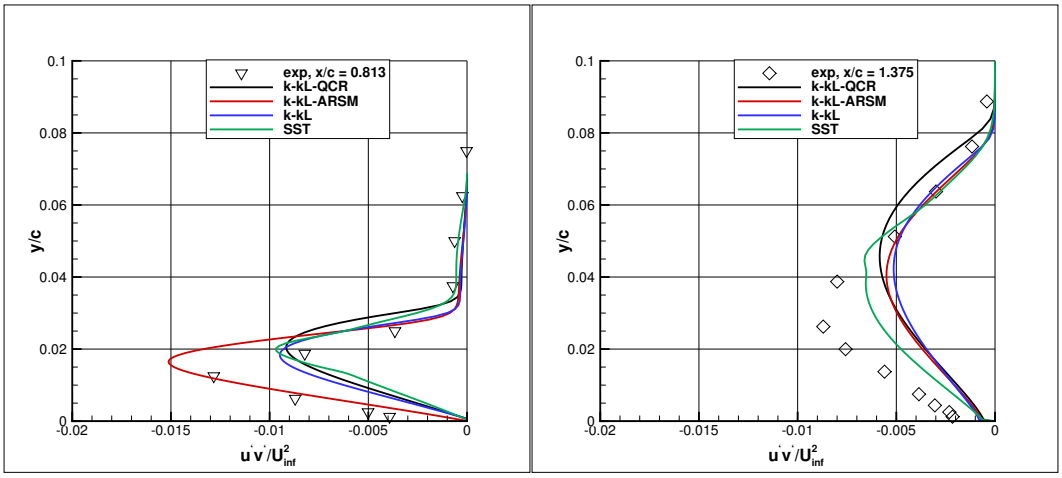


(a) x/c=0.813.

(b) x/c=1.37.

Figure 31. Axisymmetric Transonic Bump : Comparison of two-equation turbulence model shear stress results.

The corrections introduced in sections 3.4.1 and 3.4.2 should not have any effect in the results for this test case with no high-temperature or high-speed shear flow. Figure 33 shows there is no significant difference in the results using turbulence model corrections for either k-kL or k-kL-ARSM.

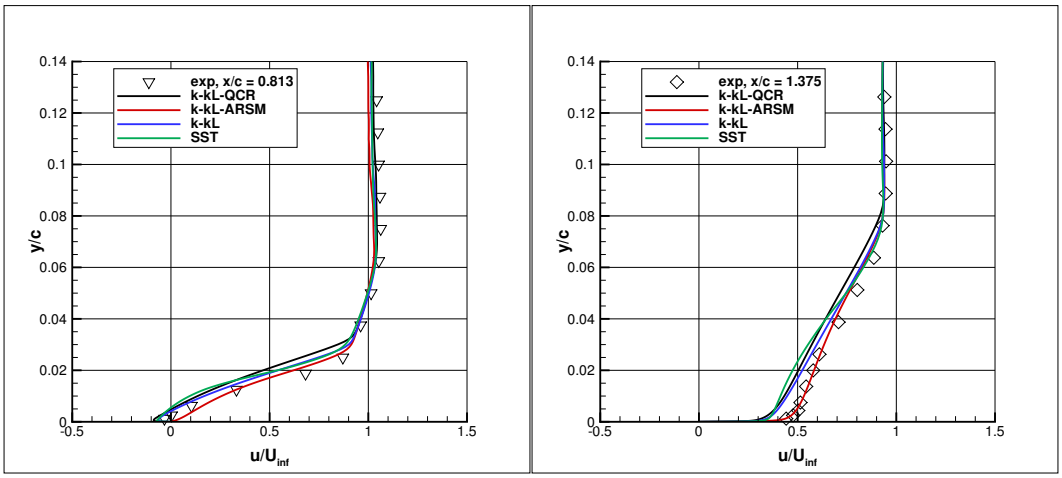


(a) x/c=0.813. (b) x/c=1.37.

Figure 32. Axisymmetric Transonic Bump : Comparison of two-equation turbulence model velocity results.

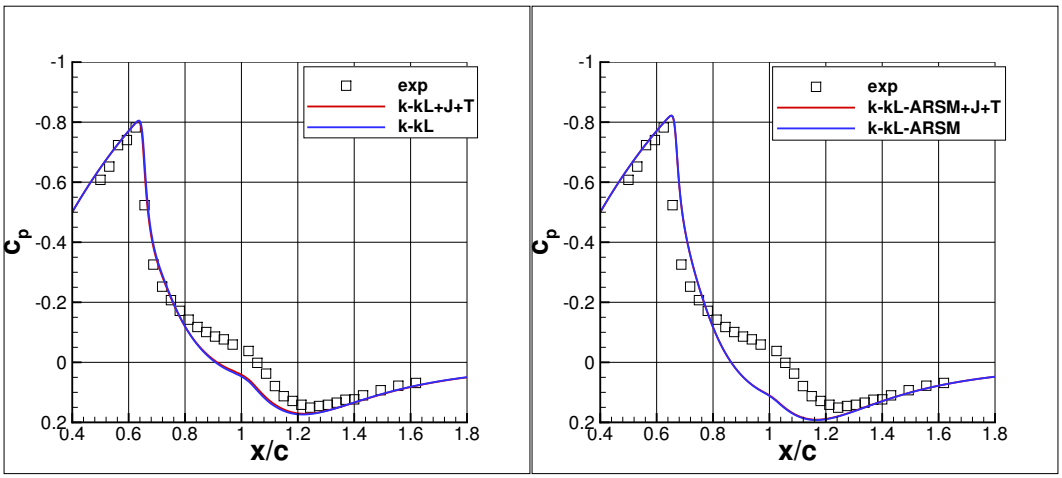


(a) k-kL. (b) k-kL-ARSM.

Figure 33. Axisymmetric Transonic Bump : effect of jet and temperature corrections.

## 4.7 Supersonic Compression Corner

This case examines supersonic flow over an axisymmetric compression corner. Experimental data are documented in references 23 and 24. Figure 34 shows the supersonic compression corner experimental configuration. The model is a 5.08 cm diameter cylinder with a 30-degree flare, which generates a shock wave. The cylinder has an upstream cusped nose designed to minimize the strength of the shocks, and data indicates that reflected shocks from the tunnel walls have no effect in the measurement region of interest. The flare is located x = 1 m downstream of the cusp-tip, allowing a turbulent boundary layer to develop upstream of the shock-wave boundary-layer interaction. The flare surface begins at x = 0.0 cm and ends at x = 5.196 cm. The test section has a Mach number of 2.85, a unit Reynolds

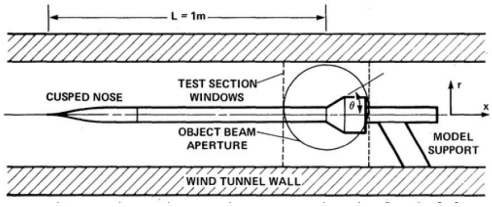


Figure 34. Supersonic Compression Corner Experimental Configuration [23].

number of 16x10$^6$/m, a stagnation pressure of 1.7 atm, and a stagnation temperature of 270 K. Figure 35(a) shows normalized pressure comparisons between two-equation kL and SST turbulence models with experimental data [22]. SST predicts the earlier location of the separation at x = -3.82 cm compared with experimental data at -2.73 cm but it produces the best pressure recovery profile in the 0 < x < 5 cm region. Figure 35(b) shows a typical Mach contour from a two-equation turbulence model. Table 7 reports the results of separation,

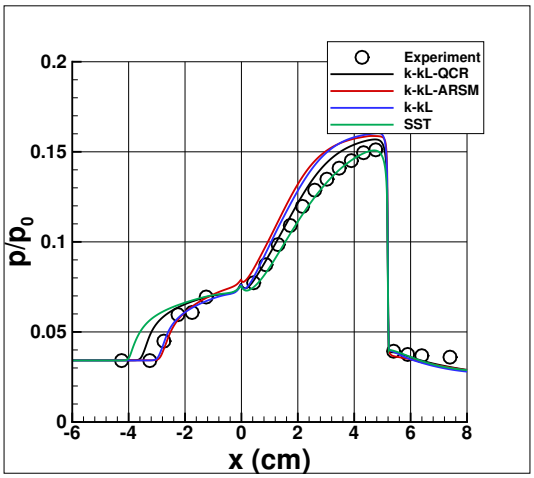


(a) Normalized pressure.

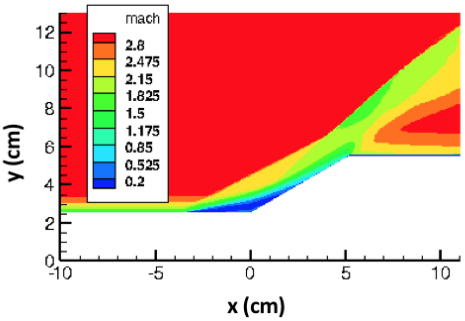


(b) Mach contour using k-kL-ARSM.

Figure 35. Supersonic Compression Corner: Comparison of kL-based turbulence models, SST and experimental data.

reattachment and bubble size using different turbulence models and experimental data. The k-kL and k-kL-ARSM produce the closest separation and reattachment locations compared with experimental data. SST shows the largest error of 60% in bubble size compared with k-kL-ARSM of 2%. The separation location is closely computed using k-kL-ARSM at x = -2.75 cm followed by RSM-kL at x = -2.68 cm and k-kL at -2.81 cm. Both SST and k-kL-QCR produced the farthest locations at -3.82 cm and -3.41 cm, respectively. Similarly, the reattachment location is better computed using k-kL-ARSM and RSM-kL. In general, the overall best results were produced using k-kL-ARSM and RMS-kL.

Next, we evaluate the capabilities of these models in predicting velocity profiles at x = -2.0 cm in the separation region and x = 1.732 cm in the reattachment region. Figure 36 shows that k-kL-ARSM improves the result at the location in the separation region. However, there are no significant improvements from any of the models in the reattachment region. The corrections introduced in sections 3.4.1 and 3.4.2 should not have any effects in the results for this test case with no high-temperature or high-speed shear flow. Figure 37 shows there is no significant difference in the results using turbulence model corrections for either k-kL

Table 7. Supersonic Compression Corner: Separation and reattachment locations.

| Results | Separation x location (cm) | Reattachment x location (cm) | Bubble Size (cm) | % Error |
|---|---|---|---|---|
| Experimental data | -2.73 | 0.97 | 3.70 | — |
| SST | -3.82 | 2.10 | 5.92 | 60.0 |
| k-kL | -2.81 | 1.34 | 4.15 | 12.1 |
| k-kL-QCR | -3.41 | 1.65 | 5.06 | 36.7 |
| k-kL-ARSM | -2.75 | 0.88 | 3.63 | 2.0 |
| RSM-kL | -2.68 | 0.72 | 3.40 | 8.2 |

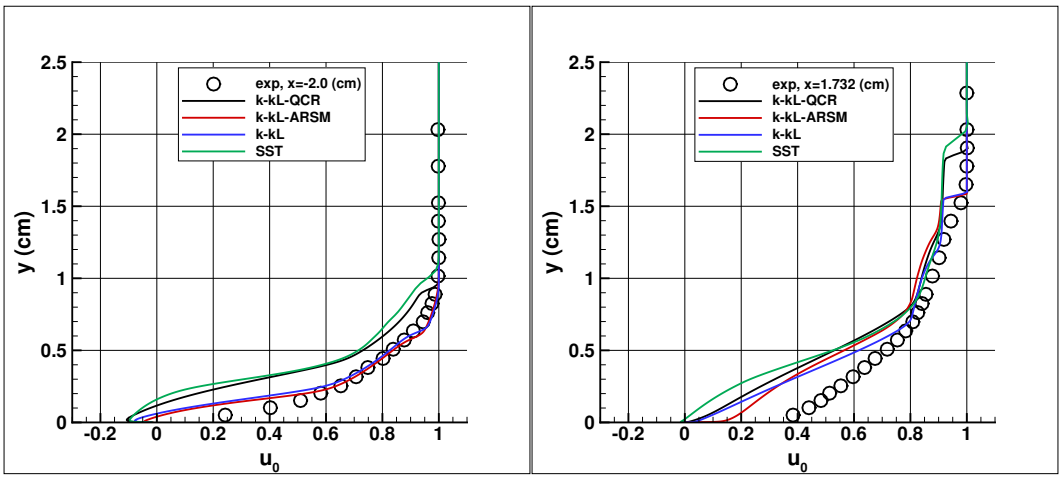


(a) x = -2.0 cm. (b) x = 1.732 cm.

Figure 36. Supersonic Compression Corner: Comparison of kL-based turbulence model, SST and experimental data.

or k-kL-ARSM.

## 4.8 Supersonic Square Duct

Computational results that use linear, nonlinear, and full Reynolds stress turbulence models based on kL are carried out for supersonic flow through a square duct. Figure 38 shows a schematic of the known secondary flow pattern in square duct flows. The flow is symmetric about the y- and z-axes so only one quadrant of the duct flow is computed. A Mach number of 3.9 and a Reynolds number based on duct diameter is 508,000. A structured grid of 81x81 in the cross-flow plane and 241 grid points in the streamwise direction was generated, which is equivalent to 1,581,201 nodes. Because the flow is complex, appropriate grid spacing near solid boundaries was maintained. The following figure (39) is a very crude representation of the in-plane velocity vectors from the experimental reference, showing one quadrant of the duct at x/D = 50. Figure 40 shows the results produced using the k-kL turbulence model. The k-kL turbulence model produces excellent convergence history with residual dropped over 14 orders of magnitude in less than 5000 iterations (see figure 40(a)). Figure 40(b) shows the cross-flow velocity patterns computed with the linear k-kL turbulence model at x/D = 50. As a typical linear RANS model, k-kL (figure 40(b)), predicts a unidirectional flow because the turbulence model cannot adequately represent the

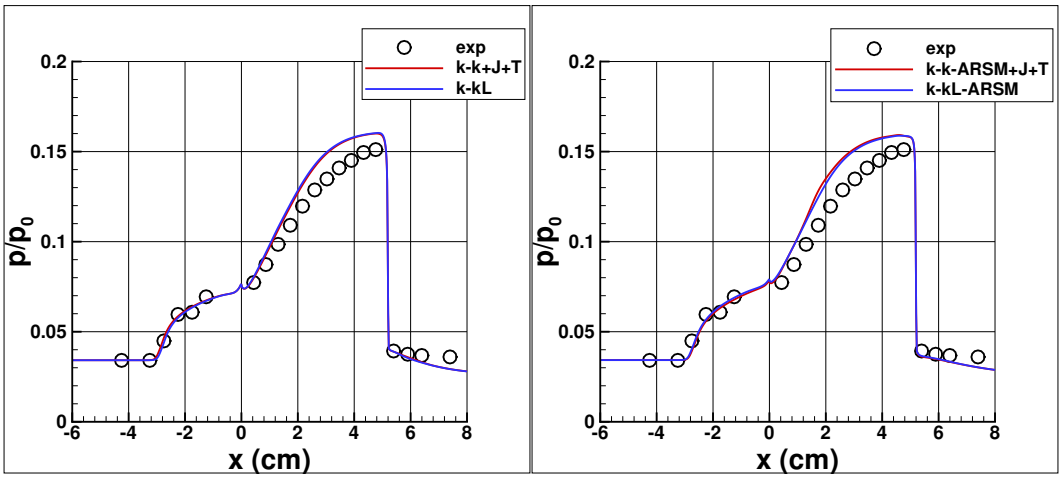


(a) k-kL. (b) k-kL-ARSM.

Figure 37. Supersonic Compression Corner:: Effect of jet and temperature corrections.

flow physics. The failure to predict cross-flow results in underproduction of the diagonal velocity at x/D = 40 and skin friction level at x/D = 50.

Figure 41 shows the results produced using the nonlinear k-kL-ARSM turbulence model. The k-kL-ARSM turbulence model produces excellent convergence history with residual dropped over 14 orders of magnitude in less than 5000 iterations (see figure 41(a)). Figure 41(b) shows the cross-flow velocity patterns computed with the k-kL-ARSM turbulence model at x/D = 50. Dramatically improved results are obtained with the nonlinear model shown in figure 41(b). The results clearly show that the secondary flows (vortices) are symmetrical about the diagonal and rotate in opposite directions. These vortices are essentially driven by the gradients of the Reynolds stresses, which cannot be simulated with the linear models and which transport net momentum toward the corner of the duct. The computed cross-flow velocity vectors that are based on the nonlinear turbulence model agree well with the experimentally observed patterns (see figure 39). In general, there are improvements in computing the diagonal velocity at x/D = 40 and skin friction level at x/D = 50.

Figure 42 shows the results produced using the nonlinear k-kL-QCR turbulence model. The k-kL-QCR turbulence model produces excellent convergence history with residual dropped over 14 orders of magnitude in less than 5000 iterations (see figure 42(a)). Figure 41(b) shows the cross-flow velocity patterns computed with the k-kL-QCR turbulence model with slightly stronger vortices than the k-kL-ARSM. Excellent agreement results are produced using the k-kL-QCR for the velocity and skin friction profiles shown in figures 42(c) and (d) at x/D = 40 and 50.

Figure 43 shows the degradation of convergence history produced using RSM-based on kL turbulence models (LRR, SSG, LRR-SSG, and LRR+C) with less than 6 orders of magnitude drop. Figure 44 shows the strong crossflow velocity patterns using RSM based on kL turbulence models (LRR, SSG, LRR-SSG and LRR+C), which are similar to nonlinear k-kL and experimental data. In general, skin friction predictions are in good agreement with experimental data (see figure 45). However, k-kL-QCR produces better predictions than any of the RSM. Figure 46 shows the vertical and diagonal velocity profiles at x/D = 40 using RSM based on kL turbulence models (LRR, SSG, LRR-SSG, and LRR+C), which are similar to nonlinear k-kL-ARSM and k-kL-QCR. However, the three RSM that use LRR coefficients are in much better agreement than the SSG results.

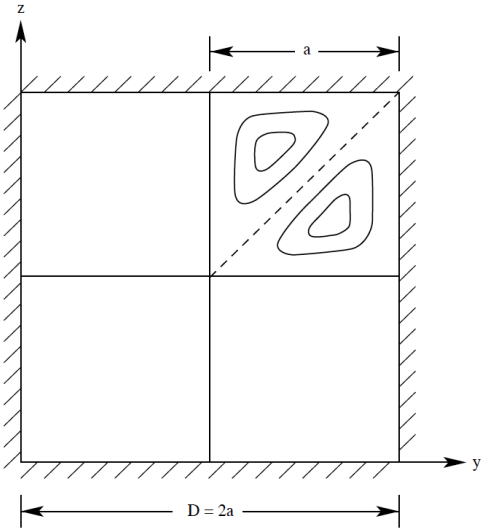


Figure 38. Experimental crossflow velocity patterns at x/D = 50 for supersonic flow through a square duct.

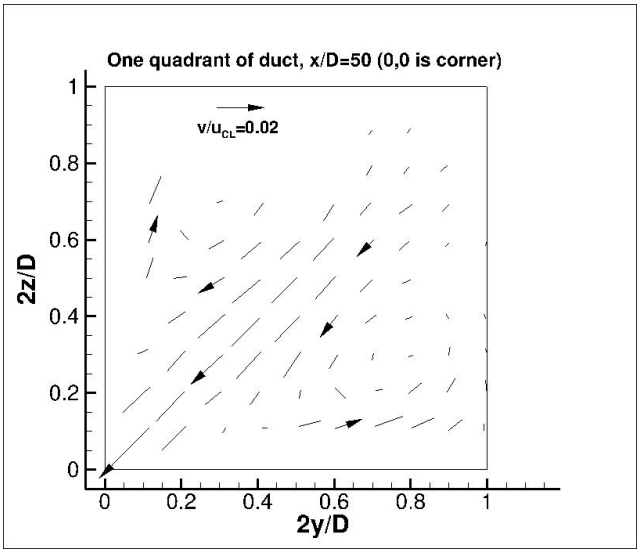


Figure 39. Secondary flow in a square duct.

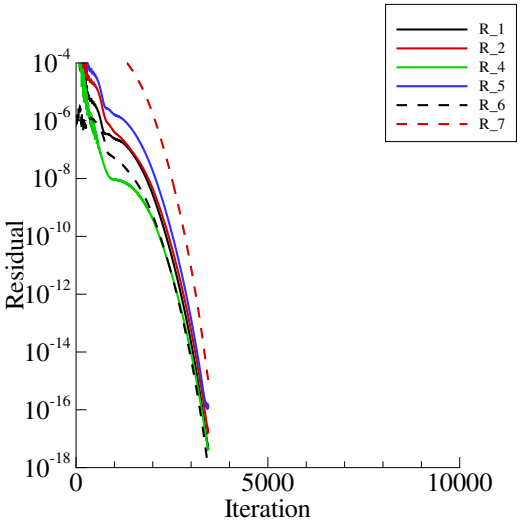


(a) Convergence history.

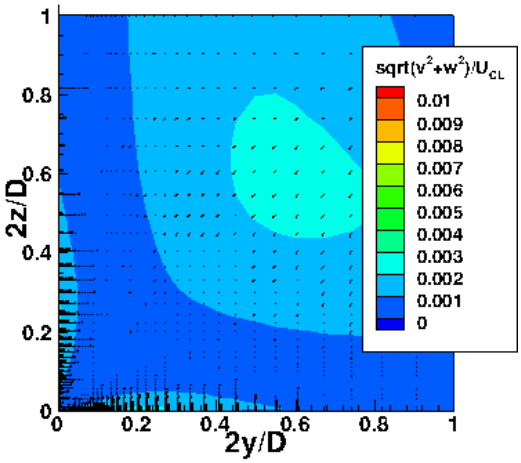


(b) Velocity vector and contour at x/D = 50.

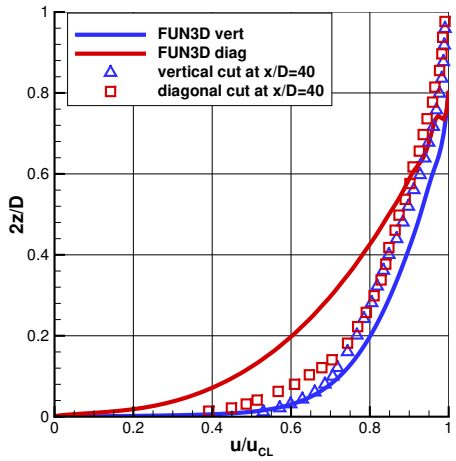


(c) Velocity at x/D = 40.

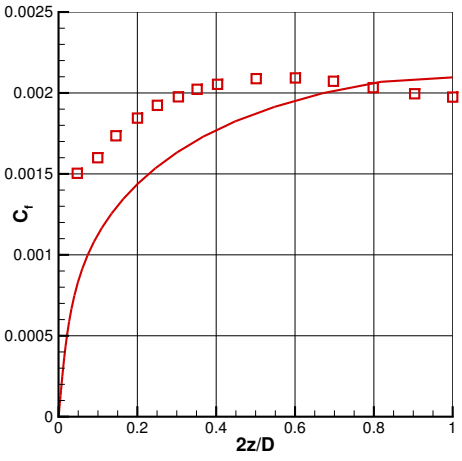


(d) Skin friction at x/D = 50.

Figure 40. 3D supersonic square duct results using the k-kL turbulence model (symbols - experimental data; line - CFD data).

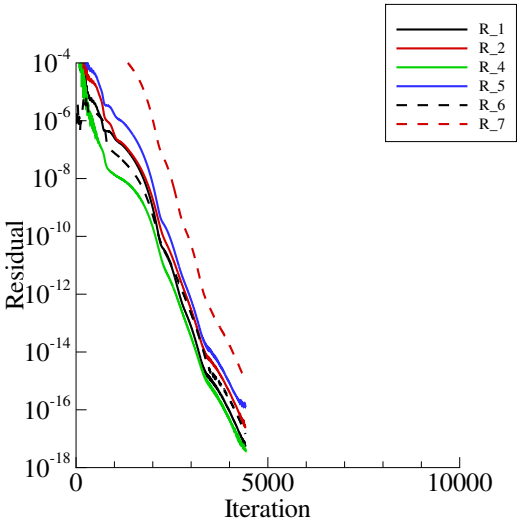


(a) Convergence history.

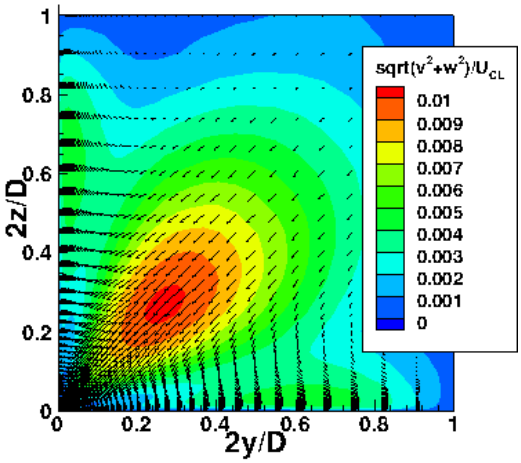


(b) Velocity vector and contour at x/D = 50.

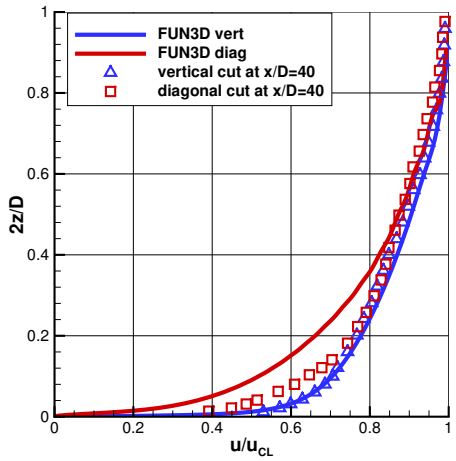


(c) Velocity at x/D = 40.

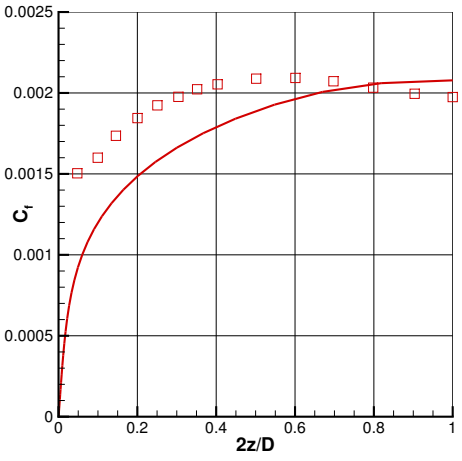


(d) Skin friction at x/D = 50.

Figure 41. 3D supersonic square duct results using the k-kL-ARSM turbulence model (symbols - experimental data; line - CFD data).

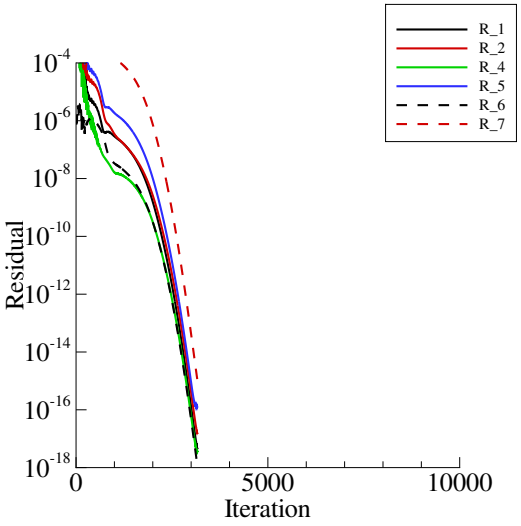


(a) Convergence history.

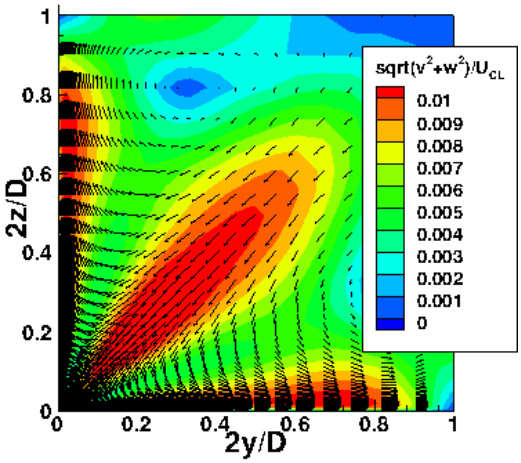


(b) Velocity vector and contour at x/D = 50.

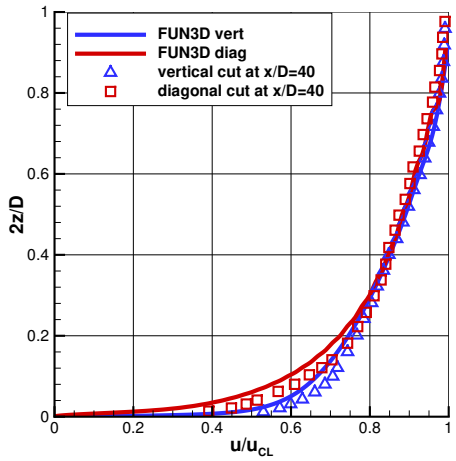


(c) Velocity at x/D = 40.

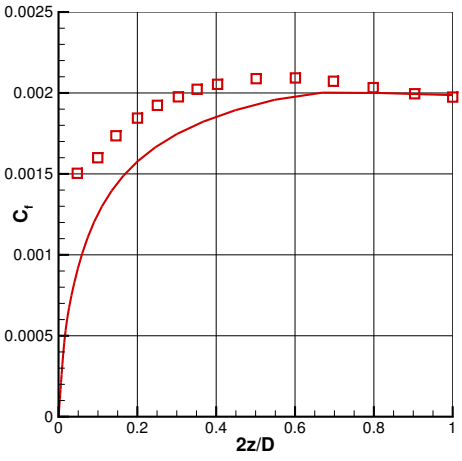


(d) Skin friction at x/D = 50.

Figure 42. 3D supersonic square duct results using the k-kL-QCR turbulence model (symbols - experimental data; line - CFD data).

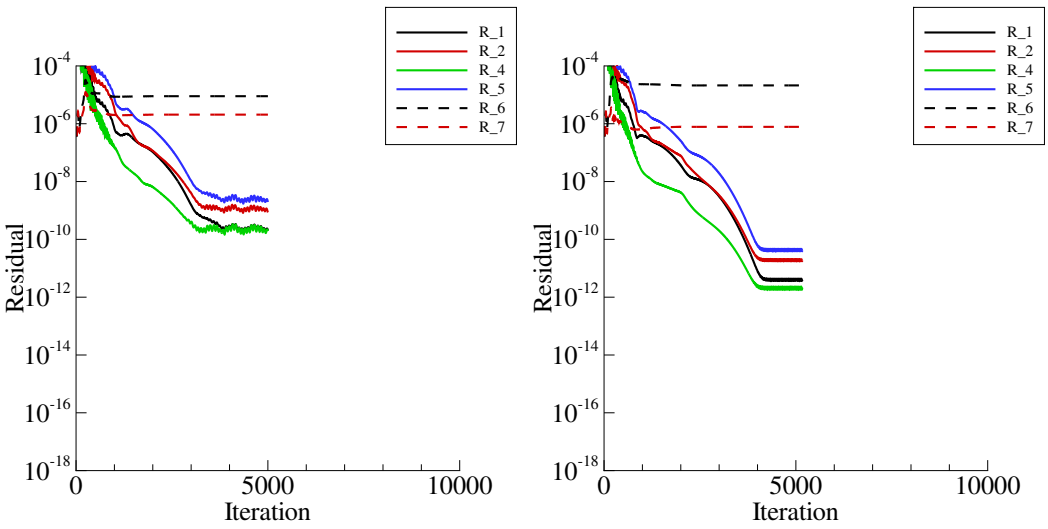


(a) LRR RSM.

(b) SSG RSM.

(c) LRR-SSG RSM.

(d) LRR+C.

Figure 43. 3D supersonic square duct convergence history results at x/D = 50, using RSM turbulence models based on kL formulation.

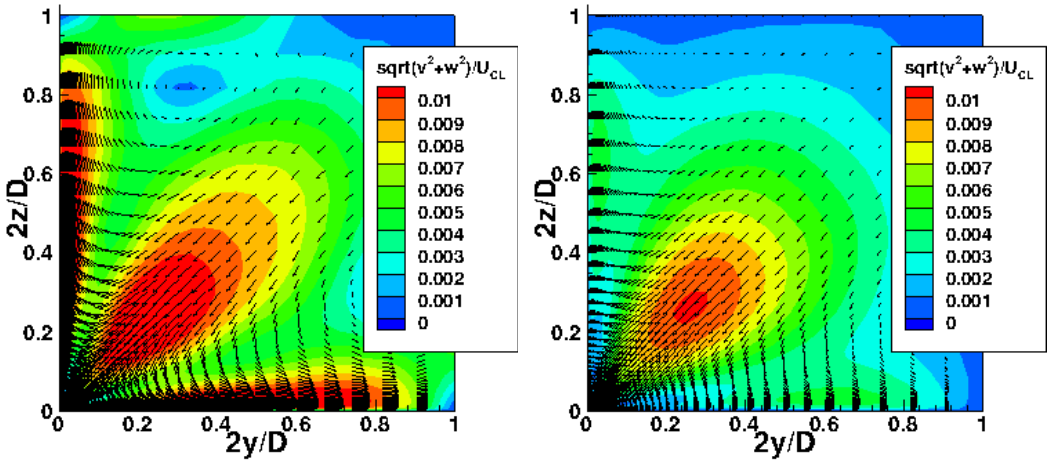


(a) LRR RSM.

(b) SSG RSM.

(c) LRR-SSG RSM.

(d) LRR+C.

Figure 44. 3D supersonic square duct velocity vector and contour results at x/D = 50, using RSM turbulence models based on kL formulation.

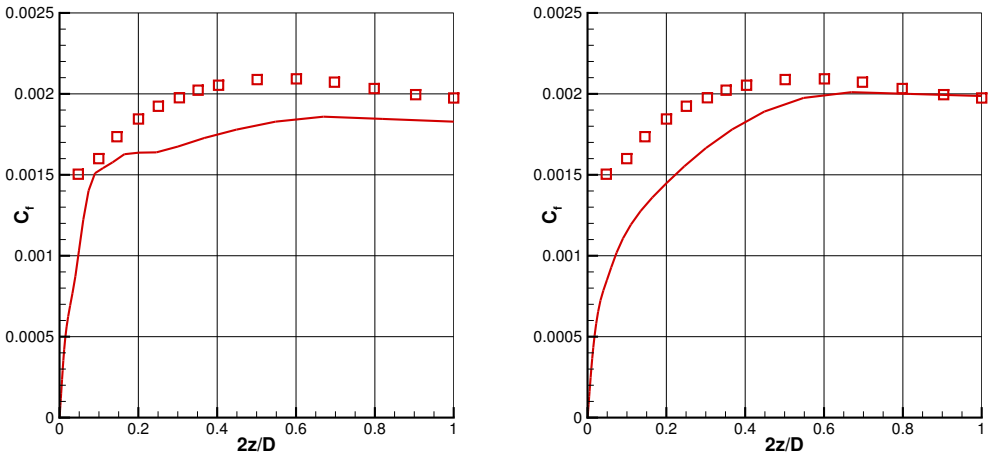


(a) LRR RSM.




(b) SSG RSM.

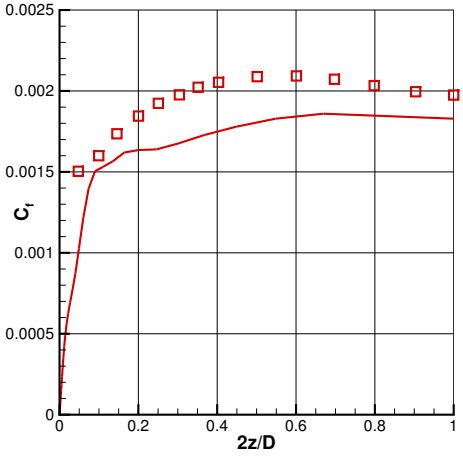


(c) LRR-SSG RSM.

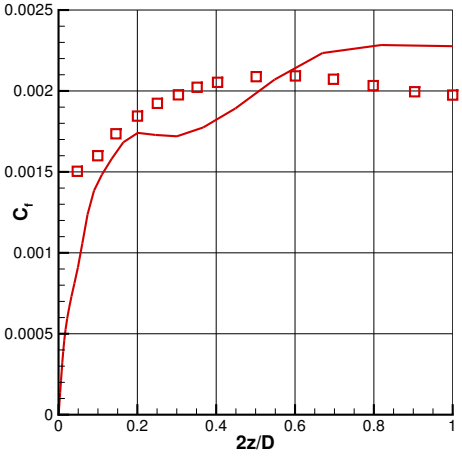


(d) LRR+C.

Figure 45. 3D supersonic square duct skin friction results at x/D = 50, using RSM turbulence models based on kL formulation (symbols - experimental data; line - CFD data).

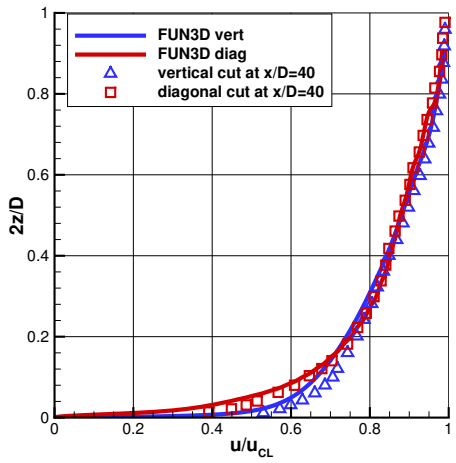


(a) LRR RSM.

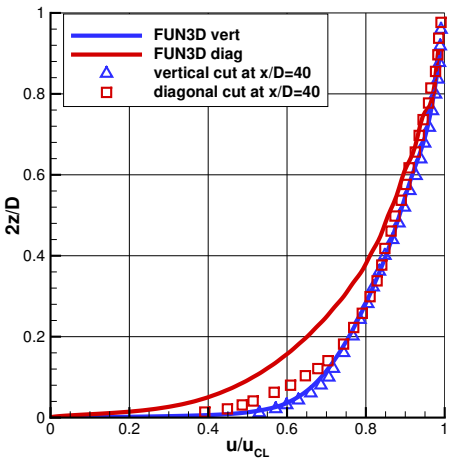


(b) SSG RSM.

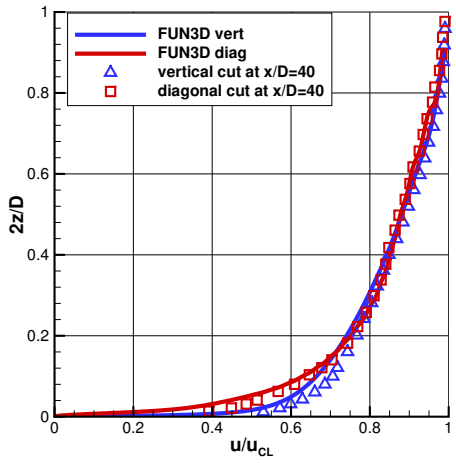


(c) LRR-SSG RSM.

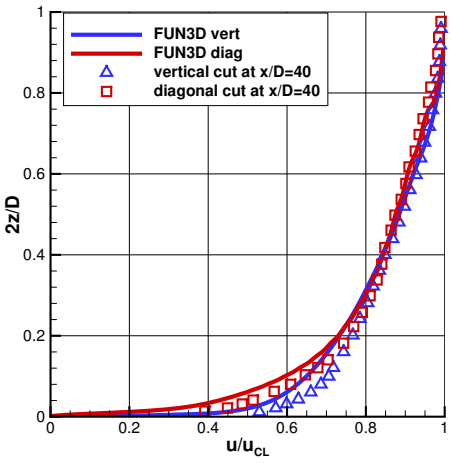


(d) LRR+C.

Figure 46. 3D supersonic square duct velocity at x/D = 40, using RSM turbulence models kL-based formulation (symbols - experimental data; line - CFD data).

# 5 Concluding Remarks

With the exception of Reynolds stress models, the turbulent kinetic energy is exclusively used as one of the transport equations in multi-equation turbulence models. The foundation of this equation is well established and accepted. The scale-determining equation, though, is considered the weakest link, even when full Reynolds stress and hybrid RANS/LES formulations are considered. The most important difference is that the kL formulation leads to a natural inclusion of higher order velocity derivatives into the source terms of the scale equation.

The present report documents the development of kL-based linear, nonlinear, and full Reynolds Stress turbulence models. A systematic investigation was conducted to assess the implementation of these models in the FUN3D CFD code utilizing several aerodynamic configurations. The computed results were compared with available experimental data and the SST turbulence model. This investigation provided significant insight into the applications and capabilities of turbulence models in the prediction of attached, separated, and corner flows.

The flat-plate test case was selected because it is the simplest of all the geometries used to generate the set of constants for the present kL-based two-equation turbulence formulation using logarithmic region requirements. The wall-mounted hump geometry presents subsonic separated flow over a smooth body. This is a simple geometry and a challenging problem for RANS eddy viscosity-based turbulence models. Typical RANS model results have more than 40% error predicting the separation bubble. These also underpredict maximum shear stress by 50% even using the full Reynolds stress turbulence models. Linear k-kL reduces the error down to 33.6%. The nonlinear k-kL-QCR did not improve any of these predictions. However, the k-kL-ARSM eliminated most of the error and RSM reduces the error down to 6.0%. Both formulations significantly improve the level of shear stress to be much closer to experimental data.

The axisymmetric transonic bump and compression corner geometries represent the next level of flow complexity because these cases contain separated flow regions that interact with a shock. The transonic case of Mach 0.875 is complex flow that proves to be challenging to most RANS turbulence models. The kL-based turbulence models reduce the results of separation bubble size from 23.7% using SST to 7.1% using RSM-kL. The improvements using the k-kL-ARSM is quite good. A supersonic flow of Mach 2.85 over a cylinder with a 30-degree flare was computed and compared with the experimental data. For this case, good agreement was obtained in predicting the surface pressure and the size of the separation bubble using the kL-based turbulence models. The error in computing the size was under 13%. The SST overpredicted the bubble size by 60%.

In the supersonic square duct, a secondary flow structure develops perpendicular to the main flow and is mainly attributed to the turbulence anisotropy, which is not simulated by linear (isotropic) models. The linear models completely failed to produce the correct characteristics for this flow. The nonlinear two-equation and full RSM models clearly captured the major trends observed in the experimental data and flow field features. The undulations that were observed represent the convecting effect of the secondary flow, undulations that were not predicted by the linear turbulence model. The jet and temperature corrections improve the results of k-kL for jet flow cases. Blending function are used to eliminate the effect of these corrections for near wall flows. These corrections do not alter any of the other results of the cases presented in this report. In a high-speed mixing layer, the spreading rates for k-kL are comparable with experimental data and much better than the results produced by SST turbulence models. In general, the k-kL-ARSM gives better agreement with experimental data than the other kL formulations and SST models for all the cases presented in this report.

# References


1. Launder, B. E. and Spalding, D. B.: *Lectures in mathematical models of turbulence*, Academic Press, London, 1972.

2. Rotta, J.: "Statistische Theorie nichthomogener Turbulenz," *Zeitschrift für Physik*, Vol. 129, No. 6, 1951, pp. 547–572.

3. Menter, F. R.; Egorov, Y. and Rusch, D.: "Steady and Unsteady Flow Modeling Using the k-$\sqrt{\text{k}}$L model," *Turbulence, Heat and Mass Transfer, 5th International symposium, Proceedings*, eds. K. Hanjalič, Y. Nagano and S. Jakirlic, Dubrovnik, Croatia, 2006, pp. 403–406.

4. Menter, F. and Egorov, Y.: "The Scale-Adaptive Simulation Method for Unsteady Turbulent Flow Predictions. Part 1: Theory and Model Description," *Flow, Turbulence and Combustion*, Vol. 85, No. 1, 2010, pp. 113–138.

5. Egorov, Y.; Menter, F.; Lechner, R. and Cokljat, D.: "The Scale-Adaptive Simulation Method for Unsteady Turbulent Flow Predictions. Part 2: Application to Complex Flows," *Flow, Turbulence and Combustion*, Vol. 85, No. 1, 2010, pp. 139–165.

6. Menter, F. R.: "Improved Two-Equation k-$\omega$ Turbulence Models for Aerodynamic Flows," NASA TM-103975, Oct. 1992.

7. Abdol-Hamid, K. S.: "Assessments of k-kl Turbulence Model Based on Menter's Modification to Rotta's Two-Equation Model," *International Journal of Aerospace Engineering*, Vol. 2015, 2015, pp. 1–18.

8. Abdol-Hamid, K. S.; Pao, S. P.; Hunter, C.; Deere, K.; Massey, S. and Elmiligui, A.: "PAB3D: It's History in the Use of Turbulence Models in the Simulation of Jet and Nozzle Flows," AIAA Paper 2006-0489, Jan. 2006.

9. Abdol-Hamid, K. S.; Carlson, J.-R. and Rumsey, C. L.: "Verification and Validation of the k-kL Turbulence Model in FUN3D and CFL3D Codes," AIAA Paper 2016-3941, Jun. 2016.

10. `http://turbmodels.larc.nasa.gov`, accessed: 2015-09-01.

11. Rumsey, C.; Smith, B. and Huang, G.: "Description of a Website Resource for Turbulence Model Verification and Validation," AIAA Paper 2010-4742, June 2010.

12. Launder, B.; Reece, G. and Rodi, W.: "Progress in the development of a Reynolds stress turbulence closure," *J. Fluid Mech.*, Vol. 68, 1975, pp. 537–566.

13. Speziale, C. G.; Sarkar, S. and Gatski, T. B.: "Modeling the pressure-strain correlation of turbulence: an invariant dynamical systems approach," *J. Fluid Mech.*, Vol. 227, 1991, pp. 245–272.

14. Hanjalic, K.: *Closure Models for Incompressible Turbulent Flows*, Von Krmn Institute, 2004.

15. Rumsey, C. and Gatski, T.: "Summary of EASM Turbulence Models in CFL3D With Validation Test Cases," NASA TM–2003-212431, June 2003.

16. Girimaji, S.: "Fully Explicit and Self-Consistent Algebraic Reynolds Stress Model," *Theoret. Comp. Fluid Dynamics*, Vol. 8, 1996, pp. 387–402.

17. Spalart, P.: "Strategies for Turbulence Modelling and Simulation,," *International Journal of Heat and Fluid Flow*, Vol. 21, 2000, pp. 252–263.

18. Coles, D.: "The law of the wake in the turbulent boundary layer," *J. Fluid Mech.*, Vol. 1, 1956, pp. 191–226.

19. Bridges, J. and Brown, C.: "Parametic Testing of Chevrons on Single Flow Hot Jets," AIAA Paper 2004-2824, 2004.

20. Goebel, S. G. and Dutton, J. C.: "Experimental Study of Compressible Turbulent Mixing Layers," *AIAA Journal*, Vol. 29, No. 4, 1991, pp. 538–546.

21. J. W. Naughton, S. A. Viken, D. G.: "Skin-Friction Measurements on the NASA Hump Model," *AIAA Journal*, Vol. 44, No. 6, 2006, pp. 1255–1265.

22. Bachalo, W. D. and Johnson, D. A.: "Transonic, turbulent boundary-layer separation generated on an axisymmetric flow model," *AIAA Journal*, Vol. 24, No. 3, 1986, pp. 437–443.

23. S. E. Dunagan, J. L. B. and Miles, J. B.: "Interferometric Data for a Shock/Wave Boundary-Layer Interaction," NASA TM–1986-88227, 1986.

24. J. Wideman, J. Brown, J. M. and Ozcan, O.: "Surface Documantation of a 3-D Supersonic, Shock Wave/Boundary Interaction," NASA TM–1994-108824, 1994.

25. Davis, D. and Gessner, F. B.: "Further Experiments on Supersonic Turbulent Flow Development in a Square Duct,," *AIAA Journal*, Vol. 27, 1998, pp. 1023–1030.

26. Roe, P. L.: "Approximate Riemann Solvers, Parameter Vectors, and Difference Schemes," *J. Comp. Phys.*, Vol. 43, 1981, pp. 357–372.

27. Batten, P.; Clarke, N.; Lambert, C. and Causon, D.: "On the Choice of Wavespeeds for the HLLC Riemann Solver," *SIAM J. Sci. Comput.*, Vol. 18, 1997, pp. 1553–1570.

28. Sun, M. and Takayama, K.: "Artificially Upwind Flux Vector Splitting Scheme for the Euler Equations," *J. Comp. Phys.*, Vol. 189, 2003, pp. 305–329.

29. Edwards, J.: "A Low-Diffusion Flux-Splitting Scheme for Navier Stokes Calculations," AIAA Paper 1996-1704, May 1996.

30. van Leer, B.: "Towards the Ultimate Conservative Difference Schemes V. A second order sequel to Godunov's Method," *J. Comp. Phys.*, Vol. 32, 1979, pp. 101–136.

31. Roe, P. L.: "Characteristic-Based Schemes for the Euler Equations," *Annual Review of Fluid Mechanics*, Vol. 18, 1986, pp. 337–365.

32. Barth, T. and Jespersen, D.: "The Design and Application of Upwind Schemes on Unstructured Meshes," AIAA Paper 1989-0366, Jan. 1989.

33. Venkatakrishnan, V.: "Convergence to Steady State Solutions of the Euler Equations on Unstructured Grids with Limiters," *J. Comp. Phys.*, Vol. 118, 1995, pp. 120–130.

34. Anderson, W. and Bonhaus, D.: "An Implicit Upwind Algorithm for Computing Turbulent Flows on Unstructured Grids," *Computers and Fluids*, Vol. 23, No. 1, 1994, pp. 1–22.

35. Anderson, W.; Rausch, R. and Bonhaus, D. L.: "Implicit/Multigrid Algorithms for Incompressible Turbulent Flows on Unstructured Grids," *J. Comp. Phys*, Vol. 128, 1996, pp. 391–408.

36. Wallin, S. and Johansson, A. V.: "An Explicit Algebraic Reynolds Stress Model for Incompressible and Compressible Turbulent Flows," *Journal of Fluid Mechanics*, Vol. 403, 2000, pp. 89–132.

37. Spalart, P.: "Direct Simulation of Turbulent Boundary Layers up to $Re_\theta = 1410$," *J. Fluid Mech.*, Vol. 187, 1988, pp. 61–98.

38. Inoue, M.: *Large-Eddy Simulation of the Flat-plate Turbulent. Boundary Layer at High Reynolds numbers*, Ph.D. thesis, California Institute of Technology, 2012.

39. M. R. Mankbadi, J. R. D. and Georgiadis, N. J.: "Large-Eddy Simulation of a Compressible Mixing Layer and the Significance of Inflow Turbulence," AIAA Paper 2017-0316, Jan. 2017.

| REPORT DOCUMENTATION PAGE | Form Approved<br>OMB No. 0704–0188 |
|---|---|

The public reporting burden for this collection of information is estimated to average 1 hour per response, including the time for reviewing instructions, searching existing data sources, gathering and maintaining the data needed, and completing and reviewing the collection of information. Send comments regarding this burden estimate or any other aspect of this collection of information, including suggestions for reducing this burden, to Department of Defense, Washington Headquarters Services, Directorate for Information Operations and Reports (0704-0188), 1215 Jefferson Davis Highway, Suite 1204, Arlington, VA 22202-4302. Respondents should be aware that notwithstanding any other provision of law, no person shall be subject to any penalty for failing to comply with a collection of information if it does not display a currently valid OMB control number.
**PLEASE DO NOT RETURN YOUR FORM TO THE ABOVE ADDRESS.**

| 1. REPORT DATE *(DD-MM-YYYY)* | 2. REPORT TYPE | 3. DATES COVERED *(From - To)* |
|---|---|---|
| 01-04-2018 | Technical Memorandum | 01/2005–12/2008 |

**4. TITLE AND SUBTITLE**

Development and Documentation of kL-Based Linear, Nonlinear, and Full Reynolds Stress Turbulence Models

**5a. CONTRACT NUMBER**

**5b. GRANT NUMBER**

**5c. PROGRAM ELEMENT NUMBER**

**6. AUTHOR(S)**

Abdol-Hamid, Khaled S.

**5d. PROJECT NUMBER**

**5e. TASK NUMBER**

**5f. WORK UNIT NUMBER**

109492.02.07.01.0$_1$

**7. PERFORMING ORGANIZATION NAME(S) AND ADDRESS(ES)**

NASA Langley Research Center
Hampton, Virginia 23681-2199

**8. PERFORMING ORGANIZATION REPORT NUMBER**

L–20912

**9. SPONSORING/MONITORING AGENCY NAME(S) AND ADDRESS(ES)**

National Aeronautics and Space Administration
Washington, DC 20546-0001

**10. SPONSOR/MONITOR'S ACRONYM(S)**

NASA

**11. SPONSOR/MONITOR'S REPORT NUMBER(S)**

NASA-TM–2018–219820

**12. DISTRIBUTION/AVAILABILITY STATEMENT**

Unclassified-Unlimited
Subject Category 02
Availability: NASA STI Program (757) 864-9658

**13. SUPPLEMENTARY NOTES**

**14. ABSTRACT**

The development and implementation of kL-based Reynolds Average Navier-Stokes (RANS) turbulence models are reported herein. The kL is based on Abdol-Hamid's closure and Menter's modification to Rotta's two-equation model. Rotta shows that a reliable transport equation can be formed from the turbulent length scale L, and the turbulent kinetic energy k. Rotta's kL equation is well suited for term-by-term modeling and displays useful features compared to other scale formulation. One of the important difference is inclusion of higher order velocity derivatives in the source terms of the scale equation. This can enhance the ability of RANS solvers to simulate unsteady flows in URANS mode. The present report documents the formulation of three model levels of turbulence models as implemented in the CFD code FUN3D. Methodology and calibration examples are shown in detail. The levels are linear k-kL and Algebraic Reynolds Stress Model (ARSM) two-equation as well as full Reynolds Stress Model (RSM). Attached, separated and corner flow cases are documented and compared with experimental, theoretical and other turbulence model data. The results show generally very good comparisons with canonical and experimental data. The results from this formulation are similar or better than results using the SST two-equation turbulence model. ARSM shows great promise with similar level of computational resources as general two equation turbulence models.

**15. SUBJECT TERMS**

CFD, Reynolds averaged, Navier-Stokes, turbulence modeling, validation, verification

| 16. SECURITY CLASSIFICATION OF: | | | 17. LIMITATION OF ABSTRACT | 18. NUMBER OF PAGES | 19a. NAME OF RESPONSIBLE PERSON |
|---|---|---|---|---|---|
| a. REPORT | b. ABSTRACT | c. THIS PAGE | | | STI Help Desk (email: help@sti.nasa.gov) |
| U | U | U | UU | 54 | 19b. TELEPHONE NUMBER *(Include area code)*<br>(757) 864-9658 |